

Spatiotemporal clustering of GHGs emissions in Europe: exploring the role of spatial component

Caterina Morelli^{1*}, Paolo Maranzano¹ and Philipp Otto²

¹*Department of Economics, Management and Statistics (DEMS), University of Milano-Bicocca, Piazza dell'Ateneo Nuovo n.1, Milano, 20126, Italy.

²School of Mathematics and Statistics, University of Glasgow, University Place, Glasgow, G12 8QQ, Scotland, United Kingdom.

*Corresponding author(s). E-mail(s): c.morelli12@campus.unimib.it;

Contributing authors: paolo.maranzano@unimib.it; philipp.otto@glasgow.ac.uk;

Abstract

In this study, we propose a novel application of spatiotemporal clustering in the environmental sciences, with a particular focus on regionalised time series of greenhouse gases (GHGs) emissions from a range of economic sectors. Utilising a hierarchical spatiotemporal clustering methodology, we analyse yearly time series of emissions by gases and sectors from 1990 to 2022 for European regions at the NUTS-2 level. While the clustering algorithm inherently incorporates spatial information based on geographical distance, the extent to which space contributes to the definition of groups still requires further exploration. To address this gap in the literature, we propose a novel indicator, namely the Joint Inertia, which quantifies the contribution of spatial distances when integrated with other features. Through a simulation experiment, we explore the relationship between the Joint Inertia and the relevance of geography in exploiting the groups structure under several configurations of spatial and features patterns, providing insights into the behaviour and potential of the proposed indicator. The empirical findings demonstrate the relevance of the spatial component in identifying emission patterns and dynamics, and the results reveal significant heterogeneity across clusters in trends and dynamics by gases and sectors. This reflects the heterogeneous economic and industrial characteristics of European regions. The study highlights the importance of the spatial and temporal dimensions in understanding GHGs emissions, offering baseline insights for future spatiotemporal modelling and supporting more targeted and regionally informed environmental policies.

Keywords: Hierarchical spatiotemporal clustering, Spatial overlapping, Clustering simulation, Greenhouse gases emissions, European regions NUTS-2

1 Introduction

The growing amount of spatiotemporal data available poses increasingly complex and intriguing challenges to researchers. In the environmental field, in particular, new technologies enable the acquisition of georeferenced data, in which spatial information is incorporated in different ways, providing a wealth of opportunities for detailed analysis. Remote sensing, GPS devices, mobile sensors, and satellite imagery generate massive spatiotemporal datasets, capturing environmental phenomena at unprecedented temporal and spatial scales. Numerous studies have focused on developing advanced spatiotemporal statistical models to predict and understand pollutant concentration behavior in different geographical areas and over time ([Calculli et al, 2015](#); [Najafabadi et al, 2020](#); [Taghavi-Shahri et al, 2020](#); [Maranzano et al, 2023](#); [Otto et al, 2024](#)) and other papers examine the effects of specific events ([Maranzano and Fassó, 2022](#); [Maranzano and Pelagatti, 2024](#)) or policies ([Maranzano et al, 2020](#)) on pollution levels. However, while the concentration of pollutants in the air has been widely studied, there remains a critical gap in the analysis of greenhouse gas (GHGs) emissions, particularly those directly resulting from human and economic activities. This lack of focus on the sources of emissions may constrain our understanding of the fundamental drivers and spatial distribution of environmental degradation. While air pollution is undoubtedly influenced by GHGs emissions, it is also shaped by various other factors, such as the morphological characteristics of the terrain, including elevation, land use, and proximity to natural barriers like mountains or water bodies. These geographical features can significantly affect the dispersion, accumulation, and concentration of pollutants in the atmosphere, adding complexity to the relationship between human activities, GHGs emissions, and localized air quality. To encourage researchers to look at air pollution from a new and challenging perspective, spatiotemporal cluster analysis offers a powerful approach to start bridging this gap, enabling the identification of spatial and temporal patterns of GHGs emissions.

Through clustering techniques, large datasets can be grouped based on the similarity of their spatial and temporal attributes, allowing researchers to discover trends, anomalies, and insights that are crucial for addressing complex environmental challenges [Birant and Kut \(2007\)](#). Spatiotemporal clustering enables the extraction of spatial and temporal relationships or similar patterns from data that is distributed over both time and space. In the context of GHGs emissions, such analysis can provide deeper insights into the spatiotemporal distribution of emissions across regions, highlight

emission hotspots, and reveal how these emissions evolve over time in response to various factors such as industrial activity and economic changes.

The application of spatiotemporal clustering has shown promise in various areas such as seismology (Georgoulas et al, 2013; Wang et al, 2006), traffic management (Jeung et al, 2008; Tietbohl et al, 2008) and risk management (Lee, 2012). In the realm of environmental science, it has been used for monitoring deforestation and vegetation distribution (Agrawal et al, 2016), water quality and sea water temperature (Alatrasta-Salas et al, 2015; Birant and Kut, 2007), tracking wildlife migration and animal behavior (Kalnis et al, 2005; Vieira et al, 2009), identifying patterns of environmental impact evaluation of firms (Morelli et al, 2025) and the interaction between climate change awareness and climate-related characteristics in different countries (Zammarchi and Maranzano, 2024).

The statistical literature proposes several methodologies of spatiotemporal cluster analysis, which are reported in a literature review proposed by Ansari et al (2020) and classified according to a taxonomy on different data types. Among all the proposed methodologies, most papers exploit density-based spatial clustering algorithm as proposed by (Ester et al, 1996) named Density-Based Spatial Clustering of Applications with Noise (DBSCAN), and its extensions (Tietbohl et al, 2008; Rocha et al, 2010; Georgoulas et al, 2013; Chen et al, 2015; Birant and Kut, 2007). Density-based clustering is able to detect clusters of arbitrary shape and different sizes without setting the number of clusters as the input parameters, but they are very sensitive to other input parameters (i.e., radius, minimum number of points, threshold).

In this paper, we rely on spatiotemporal hierarchical clustering as proposed by (Chavent et al, 2018) and extended to the spatiotemporal case by (Morelli et al, 2025). Although this approach is relatively recent, it has been widely adopted in the literature (Jaya et al, 2019; Bucci et al, 2023; Mattera and Franses, 2023; Deb and Karmakar, 2023; Morelli et al, 2025; Zammarchi and Maranzano, 2024), due to its ability to group observed units without imposing assumptions on data distribution or cluster shapes. Its flexibility is another key advantage, as it relies on a hierarchical algorithm, enabling the inclusion of any type of data by simply calculating the dissimilarity between observations using an appropriate distance measure. Another important advantage is that the version proposed by Morelli et al (2025) allows a very large number of dimensions to be input (in fact, it is possible to include time series of several variables), and the algorithm will assign different weights to the dissimilarity matrices so that the distances between observations can be explained

as much as possible. So, the algorithm will only take into account information that is useful for identifying clusters. In this context, we propose a measure designed to evaluate the contribution of one dissimilarity matrix relative to others, with the specific goal of assessing the role of the spatial component when combined with distances calculated from other variables. After providing a theoretical explanation of this measure, supported by examples of hypothetical scenarios, we demonstrate its behavior through a simulation experiment. This experiment explores how the measure responds to variations in the spatial distance between clusters and their degree of overlap in space.

This measure is fundamentally important, not only in our specific application but also in other contexts. Given that cluster analysis is a form of exploratory analysis applied to data whose characteristics are not yet fully understood, it is not appropriate to a priori include the spatial component (or other variables describing distinct phenomena) and force the algorithm to consider all input information equally. Instead, it is crucial to understand the actual role of spatial information, especially when it is associated with a specific phenomenon that has not yet been examined through a spatiotemporal approach.

The contributions of this paper are twofold, addressing both methodological innovation and practical application in the environmental domain. From a methodological perspective, we introduce a novel measure to assess the role of the spatial component in clustering, particularly when it is combined with dissimilarities derived from other variables. This measure provides a valuable tool for understanding the influence of spatial information on clustering outcomes and serves as a foundation for future analyses involving spatiotemporal data. From an application standpoint, we approach the environmental issue of GHGs emissions from a fresh perspective, offering insights into the patterns and dynamics of emissions across regions and over time. A key objective is to evaluate the relevance of spatial information in identifying these patterns, thereby contributing to a deeper understanding of GHGs emissions and their spatial-temporal distribution.

The relevance of these results extends to both policymakers and statisticians. For policymakers, the insights gained from this analysis are instrumental in formulating localized strategies to mitigate GHGs emissions, enabling more targeted and effective interventions. For statisticians in the environmental field, this study provides a baseline analysis that highlights critical factors to consider when modeling GHGs emissions data. Specifically, it underscores the importance of incorporating spatial and temporal dimensions and offers guidance on whether spatiotemporal models are necessary for

accurate representation and prediction. Together, these contributions lay the groundwork for more robust and nuanced approaches to addressing pressing environmental challenges.

The rest of the paper is structured as follows: in Section 2, we describe the methodology proposed by [Chavent et al \(2018\)](#) and [Morelli et al \(2025\)](#), in Section 3, we provide the methodological contribution of the paper, in Section 4 we present the simulation experiment on the performance of spatiotemporal clustering algorithm and the measure to assess the role of the spatial component and in 5 we discuss the empirical findings, thus the clusters obtained from the algorithm and the contribution of the spatial distances.

2 Spatiotemporal hierarchical clustering

In this section, we briefly recall the baseline methodology proposed by [Chavent et al \(2018\)](#), in which two dissimilarity matrices, one containing spatial information and the other containing clustering features, are combined to cluster the units under some geographical constraint. Then, we describe the extension proposed by [Morelli et al \(2025\)](#), which considers a spatiotemporal framework and adds a novel algorithm for the identification of the weights for the spatial and non-spatial matrices. Finally, we propose a metric that allows us to evaluate the role of the spatial component in explaining the dissimilarity of the data and, thus, the relevance of the spatial information with respect to the features used in the cluster analysis.

2.1 Baseline methodology: spatial hierarchical clustering

Let $D_0 = [d_{0,ij}]_{i,j=1,\dots,n}$ and $D_1 = [d_{1,ij}]_{i,j=1,\dots,n}$ refer respectively to any distances matrix of variables and the spatial distances matrix considering a sample of n units. Also, let w_i with $i = 1, \dots, n$ be the weight of the i -th cross-sectional unit to be clustered. When no prior information is available, the weight is commonly set to $w_i = 1/n$. In order to account for different measurement scales, it is necessary to scale D_0 and D_1 with respect to their maximum values so that the clustering distances across observations take values between 0 and 1. In the spatial clustering proposed by [Chavent et al \(2018\)](#), the matrices D_0 and D_1 are combined through a convex combination with parameter α , which provides the weight of geographical information in determining the clusters. When the mixing parameter is null, that is, when $\alpha = 0$, in the linear combination of the dissimilarity matrices $D(\alpha) = (1 - \alpha)D_0 + \alpha D_1$, the geographical dissimilarities are not taken into account,

while when $\alpha = 1$ the features distances are ignored, and the clusters are defined only based on the geographical distances.

Once the combined matrix D is obtained, the Ward hierarchical clustering algorithm (Ward, 1963) is applied to cluster the units. In its original formulation, it starts with an initial partition into n clusters of singletons, and at each step, the algorithm aggregates the two clusters such that the new partition has minimum within-cluster inertia. In our context, given a partition $\mathcal{P}_K^\alpha = (C_1^\alpha, \dots, C_K^\alpha)$ into K clusters, the mixed pseudo-inertia for cluster C_K^α is defined as the convex combination of the sum of square dissimilarities in D_0 and D_1 across the units belonging to cluster C_K^α . The corresponding mixed pseudo-inertia, denoted as $I(C_K^\alpha)$, is computed as

$$I(C_K^\alpha) = (1 - \alpha) \sum_{i \in C_K} \sum_{j \in C_K} \frac{w_i w_j}{2 \sum_{i \in C_K} w_i} d_{0,ij}^2 + \alpha \sum_{i \in C_K} \sum_{j \in C_K} \frac{w_i w_j}{2 \sum_{i \in C_K} w_i} d_{1,ij}^2 \quad (1)$$

The overall pseudo-within-cluster inertia of the partition to be minimized is obtained as the sum of the pseudo-inertia of each cluster and, thus, is computed as follows

$$W_\alpha(\mathcal{P}_K^\alpha) = \sum_{k=1}^K I_\alpha(C_k^\alpha). \quad (2)$$

The algorithm aims to identify the cluster partition such that units in the same clusters have a lower total square dissimilarity. Before proceeding, we point out that pseudo-inertia is a generalization of inertia, where the dissimilarities can be either Euclidean or non-Euclidean. From here on, with a slight abuse of notation, we will refer to inertia in substitution of the pseudo-inertia.

The main issue in the hierarchical clustering methodology concerns the choice of the mixing parameters α and the number of clusters K . Chavent et al (2018) suggest setting a prior value for K and then finding α such that it allows to explain the same proportion of the dissimilarities from both matrices, with respect to the cases in which the clusters are obtained considering only the feature matrix or the spatial matrix. In order to clarify their approach, we recall the notion of the proportion of the total inertia explained by partition \mathcal{P}_K^α in D_0 and D_1 for K clusters, which is computed as

$$Q_{D_0}(\mathcal{P}_K^\alpha) = 1 - \frac{W_{D_0}(\mathcal{P}_K^\alpha)}{W_{D_0}(\mathcal{P}_1)} \quad Q_{D_1}(\mathcal{P}_K^\alpha) = 1 - \frac{W_{D_1}(\mathcal{P}_K^\alpha)}{W_{D_1}(\mathcal{P}_1)} \quad (3)$$

Specifically, $Q_{D_0}(\mathcal{P}_K^\alpha)$ quantifies the proportion of inertia from features dissimilarities (i.e., $W_{D_0}(\mathcal{P}_1)$) explained by partition \mathcal{P}_K^α , while $Q_{D_1}(\mathcal{P}_K^\alpha)$ quantifies the amount of geographical inertia (i.e., $W_{D_1}(\mathcal{P}_1)$) explained by partition \mathcal{P}_K^α .

To account for potential scale issues in $Q_{D_0}(\mathcal{P}_K^\alpha)$ and $Q_{D_1}(\mathcal{P}_K^\alpha)$, the $Q_\beta(\mathcal{P}_K^\alpha)$ metrics are then normalized with respect to the baseline case of purely-geographical or purely-features clustering, that is, by computing the following ratios:

$$\tilde{Q}_{D_0}(\mathcal{P}_K^\alpha) = \frac{Q_{D_0}(\mathcal{P}_K^\alpha)}{Q_{D_0}(\mathcal{P}_K^0)} \quad \tilde{Q}_{D_1}(\mathcal{P}_K^\alpha) = \frac{Q_{D_1}(\mathcal{P}_K^\alpha)}{Q_{D_1}(\mathcal{P}_K^1)}. \quad (4)$$

This relative formulation allows for a straightforward interpretation of the values. For a given K and a given mixing parameter α , the formulas are expressing the percentage of the explained proportion of inertia in features (or spatial) dissimilarity matrix obtained by using a mixture of features and geographical information to generate the partition \mathcal{P}_K^α (i.e., $Q_{D_0}(\mathcal{P}_K^\alpha)$ (or $Q_{D_1}(\mathcal{P}_K^\alpha)$)) with respect to the proportion of inertia that would be explained by only using features (or spatial) dissimilarities to generate the partition \mathcal{P}_K^0 (or \mathcal{P}_K^1) in K clusters (i.e., $Q_{D_0}(\mathcal{P}_K^0)$ (or $Q_{D_1}(\mathcal{P}_K^1)$)). For a deeper understanding and comprehensive discussion about the properties of these quantities, we refer the readers to Section 3 in [Chavent et al \(2018\)](#).

[Chavent et al \(2018\)](#) suggest to choose α such that the normalized proportion of the explained pseudo inertia from D_0 and D_1 are as similar as possible, that is,

$$\min_\alpha |\tilde{Q}_{D_0}(\mathcal{P}_K^\alpha) - \tilde{Q}_{D_1}(\mathcal{P}_K^\alpha)|. \quad (5)$$

In other words, this means finding α such that the proportion of explained pseudo inertia attributed to the features and the spatial information is as close as possible. Specifically, this ensures that the proportion of inertia explained when using only features or only spatial information to generate the partition is similar. To select the number of clusters K , [Chavent et al \(2018\)](#) suggest to choose it a priori. Similarly, [Mattera and Franses \(2023\)](#) set an initial number of clusters K_0 considering the partition associated with D_0 , then they determine α as in [Chavent et al \(2018\)](#), and finally they define the optimal number of clusters based on the combined dissimilarity matrix.

Notice that this selection method does not always allow to identify α such that it captures the highest possible overall dissimilarity in the data. To address such drawback, [Jaya et al \(2019\)](#) start

finding α according to [Mattera and Franses \(2023\)](#), and they end up choosing a different value for the mixing parameter in order to explain better the proportion of inertia in one matrix, with a relatively small reduction of the proportion of inertia from the other matrix.

Moreover, the algorithm is induced to select a combination of matrices such that both D_0 and D_1 are always included, without knowing if and how much the geographic component is really relevant in the cluster formation. In other words, we do not know what role spatial distance plays in the representation of the phenomenon we are examining. This is a very important point since cluster analysis is used as exploratory analysis, so it could be applied when we start studying new or little-analyzed variables in literature, and we often do not have a large amount of previous knowledge. It would, therefore, be preferable to apply a methodology that allows the geographical distance between observations to be considered only when providing some actual improvements in the clustering results.

2.2 Spatiotemporal hierarchical clustering

In [Morelli et al \(2025\)](#), the authors introduced an enhanced version of spatial hierarchical clustering that allows the use of more than two dissimilarity matrices. Also, they identify the optimal combination of these matrices which maximizes the gain induced by using a mixed approach instead of a purely spatial and non-spatial approach in terms of proportion of explained inertia within the clusters without forcing the algorithm to include all the input matrices in the final combination. Such principle holds for both the spatial and non-spatial information.

The need to incorporate multiple dissimilarity matrices arose from our objective of analyzing a dataset consisting of time series for more than one variable and the geographic coordinates of individual units. Indeed, the approach proposed by [Chavent et al \(2018\)](#) allows for the construction of a single matrix containing the Euclidean distances of variables observed at a given moment or a matrix representing the distances between time series for a single variable ([Bucci et al, 2023](#); [Deb and Karmakar, 2023](#); [Mattera and Franses, 2023](#)). When dealing with multiple time series, it becomes necessary to compute a dissimilarity matrix for each variable observed over a given period. Therefore, the challenge lies in combining more than two matrices. Notice that the methodology is not limited to spatiotemporal data but can be applied to any scenario where high-dimensional data requires the combination of more than two dissimilarity matrices. Nevertheless, this approach has

been developed specifically to address the need for identifying patterns and dynamics in phenomena where both temporal evolution and geographic location are critical.

Let $D_p = [d_{p,ij}]_{p=1,\dots,P-1;i,j=1,\dots,n}$ being the dissimilarity matrices containing the distances across time series for P variables for n units. Let us assume that the first $P - 1$ matrices are associated with non-spatial features or time series and let $D_P = [d_{P,ij}]_{i,j=1,\dots,n}$ refer to the spatial (or geographical) dissimilarity matrix across the n units, which is typically computed as geodetic distances between coordinates. Moreover, we recall that dissimilarity matrices are normalized with respect to their maximum value. The main issue here is to find a suitable combination of the two clustering hyperparameters, namely the number of group K , and the weighting vector $\underline{\alpha} = [\alpha_p]_{p=1,2,\dots,P} = (\alpha_1, \alpha_2, \dots, \alpha_p, \dots, \alpha_P)$ with $\alpha_p > 0 \quad \forall p = 1, \dots, P$ and such that $\sum_{p=1}^P \alpha_p = 1$. Notice that, although the grid can be either regular or irregular, we suggest using a regular grid with constant step $\Delta\alpha$. Let us define a range of number of clusters from $K = 1$ to $K = K_{max}$ and for each $K = 1, \dots, K_{max}$ consider all the possible combinations for a grid of $\underline{\alpha}$. For each combination of K and $\underline{\alpha}$ we compute the corresponding convex linear combination of dissimilarity matrices $D(\underline{\alpha}) = \sum_{p=1}^P \alpha_p D_p$ and we identify the clustering partition \mathcal{P}_K^α according to the Ward hierarchical algorithm.

Following the criterion defined in [Morelli et al \(2025\)](#), for every $K = 1, 2, \dots, K_{max}$ we choose the optimal weighting vector $\underline{\alpha} = \underline{\alpha}^*$ which maximizes the weighted average of the explained mixed inertia¹ induced by the partition, given by

$$\bar{Q}(\mathcal{P}_K^\alpha) = 1 - \frac{\sum_{p=1}^P W_{D_p}(\mathcal{P}_K^\alpha)}{\sum_{p=1}^P W_{D_p}(\mathcal{P}_1^\alpha)}. \quad (6)$$

Its value ranges between 0 and 1, reaching its maximum when partition \mathcal{P}_K^α allows us to explain the total dissimilarity in each matrix. The optimization step conditioning on K is iterated across a user-defined range of number of clusters $K = 1, 2, \dots, K_{max}$ evaluated at the corresponding optimal $\underline{\alpha}_K^*$. Finally, the optimal number of clusters $K = K^*|\underline{\alpha}_K^*$ is determined according to a user-defined set of clustering criteria, such as the increments in the weighted average proportion of explained inertia induced by the increase in the number of clusters and the Silhouette index ([Morelli et al, 2025](#)), the Dunn's index, the C-index, the Calinski-Harabasz's index, and the McClain-Rao's index

¹We refer the reader to the detailed discussion in [Morelli et al \(2025\)](#) about the analytics and the interpretation of the weighted average of explained mixed pseudo inertia, in particular to its link with the gain in using a mixed approach compared to the purely non-spatial or purely spatial cases.

(Zammarchi and Maranzano, 2024). In this paper, we consider only the increments in the weighted average proportion of explained inertia.

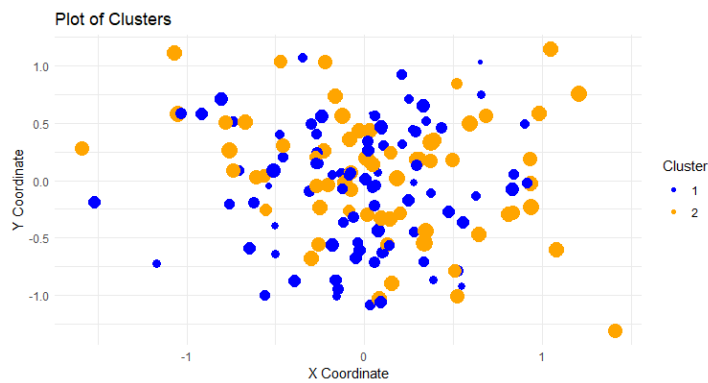
3 The role of the spatial component in hierarchical clustering

Previously, we mentioned that a key advantage of the multi-matrix algorithm is that the choice of the weighting vector $\underline{\alpha}$ does not necessarily require the inclusion of the spatial component but rather incorporates it only when it contributes meaningfully to explaining the overall dissimilarity in the data. However, it is important to note that the weight assigned to the spatial component cannot be interpreted as a direct measure of its relevance. While it may be intuitive to think that as the spatial weight α_P increases, the explained inertia (and thus the proportion and normalization) also increases, it remains unclear how these quantities grow relative to each other. Indeed, if the increase in inertia were proportional to the weights of the matrices, the optimal configuration for Chavent et al (2018) would always result in $\alpha_P = 0.5$, and the optimal outcome for Morelli et al (2025) could be any value for α_P .

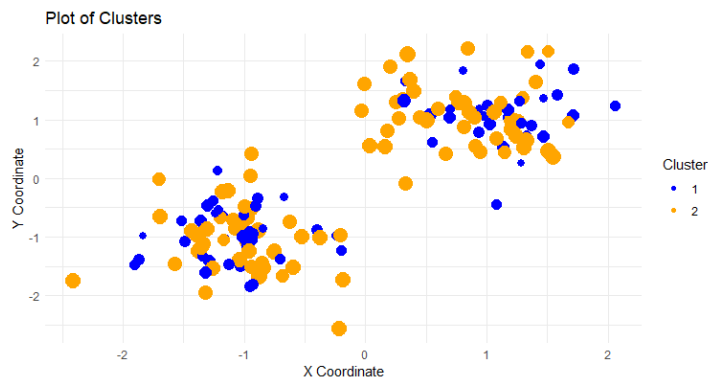
To illustrate this unclear behavior, we provide three simulated numerical examples (or scenarios) in which the spatial component is either (a) completely irrelevant, (b) relevant but not related to the phenomenon, or (3) relevant and useful in describing the phenomenon². Without losing generalities, let us consider the case with only two dissimilarity matrices, the first containing the spatial distances and the second collecting the Euclidean distances across observations for a single feature. In Figure 1, we provide a graphical representation of the three above scenarios.

In the first case, the clusters present high dissimilarities related to the features, but they perfectly overlap with respect to the spatial coordinates. As the spatial component is not playing any role in describing the phenomenon and is not useful in maximizing the explained inertia, it will be not included in the final optimal combination of weights. In the second scenario, the partition obtained using only the features dissimilarity matrix is completely different from the one obtained using only the spatial dissimilarities. Here, the spatial component leads to the identification of groups that are well separated in space but are not related to the actual pattern of the phenomenon under study. Therefore, we expect the algorithm to return as optimal mixing parameter either $\alpha = 0$ or $\alpha = 1$,

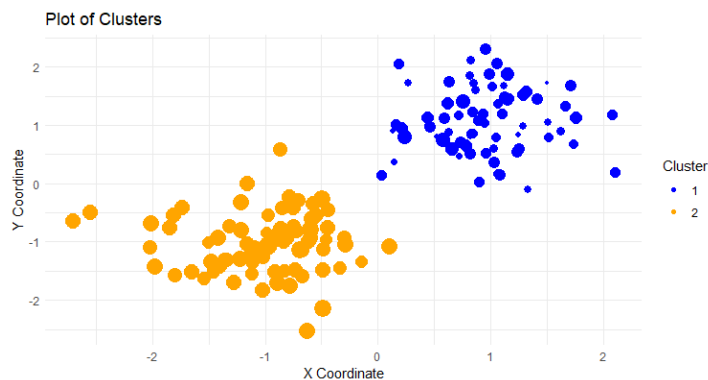
²Notice that the statement "the spatial component is relevant with respect to the phenomenon" refers to whether the spatial/geographical distribution of the units to be clustered is related to the phenomenon under study and thus can be useful for the purpose of adequately constructing clusters ("it is relevant for the clustering") or is unrelated to the underlying phenomenon and thus does not contribute in a useful way to the construction of clusters ("it is not relevant for the clustering").



(a)



(b)



(c)

Fig. 1: Example of clusters defined under different spatial conditions. In panel (a), the spatial component is not relevant: observations from different clusters present the same spatial distribution, and clusters are perfectly overlapping in space. In panel (b), the spatial component is relevant but not related to the phenomenon: it is possible to identify groups according to spatial distances, but this is not useful in describing the phenomenon because, in each spatial cluster, we can find observations with different features. In panel (c), the spatial component is relevant and related to the phenomenon: we can identify the same clustering partition either using spatial dissimilarities or feature dissimilarities.

depending on which matrix explains a greater portion of the dissimilarity across clusters. In the third scenario, the cluster partition obtained from observing only the features is identical to the one

obtained using only the spatial component. Thus, the geographical distribution is strongly related to the phenomenon of interest and will play a crucial role in building the clusters. In this latter case, the spatial component's role is clearly significant, yet any value of α would suffice to maximize the weighted average explained inertia because if the clustering algorithm on D_0 leads to the same partition obtained using only D_1 , any combination of D_0 and D_1 will lead to the same results.

The above simulated example shows that the weight of the spatial component, represented by α , cannot be interpreted as a measure of the actual importance of geographical information for identifying the groups of observations that characterize the patterns of the examined variables. Indeed, it is only the solution obtained from a maximization task. On the one hand, when the spatial component is included in the combined dissimilarity matrix D , thus $1 - \alpha > 0$, or $\alpha_P > 0$ in multidimensional case, this indicates that spatial information is at least partially relevant in explaining the phenomenon. On the other hand, when the spatial information became more and more related to the dissimilarities across features, that is, D_0 and D_1 lead to similar clustering partitions, it is no longer necessary to include the spatial component because feature dissimilarities are able to capture a high proportion the inertia in the spatial dissimilarities and vice versa.

To properly understand the role of the spatial dissimilarity matrix in relation to the phenomenon under study, it is more appropriate to examine how the explained inertia in the resulting clusters changes when combining the two dissimilarity matrices with respect to the cases in which the features or spatial distances are used independently. The normalized proportion of explained inertia defined by [Chavent et al \(2018\)](#) (Equation 4) is particularly useful for this purpose because it provides the percentage of explained variability in the clustering partition obtained from the combined dissimilarity matrix with respect to the case in which the partition is obtained from one dissimilarity matrix only.

When we choose to incorporate the spatial component, we effectively renounce to a proportion of the inertia explained by the features to gain a certain amount of inertia explained within the spatial component. It follows that the actual contribution of the geographical information can be well approximated by the difference between the normalized proportion of inertia explained by the spatial component within the mixed cluster partition and the reduction in the normalized proportion of inertia explained by the features that results from including the spatial component. Specifically, in the case where there are only two matrices D_0 and D_1 , we quantify the importance of spatial

features through a novel indicator, namely the Joint Inertia of partition \mathcal{P}_K^α , which is computed as

$$JI(\mathcal{P}_K^\alpha) = \tilde{Q}_{D_1}(\mathcal{P}_K^\alpha) - (1 - \tilde{Q}_{D_0}(\mathcal{P}_K^\alpha)) = \frac{Q_{D_1}(\mathcal{P}_K^\alpha)}{Q_{D_1}(\mathcal{P}_K^1)} + \frac{Q_{D_0}(\mathcal{P}_K^\alpha)}{Q_{D_0}(\mathcal{P}_K^0)} - 1 \quad (7)$$

The generalization to the case of multiple dissimilarity matrices, one of which relates to the spatial component, is straightforward. Recalling the notation previously introduced, let us consider the generic partition induced by a given combination of mixing parameters (i.e., \mathcal{P}_K^α) and let $D_{-P} = [d_{p,ij}]_{p=1,\dots,P-1;i,j=1,\dots,n}$ be the dissimilarity matrices containing the distances across the $P-1$ time series for n units and let $D_P = [d_{p,ij}]_{i,j=1,\dots,n}$ be the spatial dissimilarity matrix across the n units, which may be computed as geodetic distances between coordinates. Let $\underline{\alpha} = [\alpha_p]_{p=1,2,\dots,P}$ be the vector of mixing weights used to compute the linear combination of dissimilarity matrices $D(\underline{\alpha}) = \sum_{p=1}^P \alpha_p D_p$ such that $\sum_{p=1}^P \alpha_p = 1$. Moreover, let us define the matrix $D_{-P}(\underline{\alpha}|\alpha_P = 0) = \sum_{p=1}^{P-1} \alpha_p D_p$ as the combination of the $P-1$ dissimilarity matrices excluding the spatial matrix D_P , and the resulting clustering partition $\mathcal{P}_K^{\alpha-P}$. Similarly, define the partition obtained by using only the spatial information (i.e., by fixing $\alpha_P = 1$) as $\mathcal{P}_K^{\alpha_P=1}$.

If we compute the optimal weighting vector obtained by the combination of the non-spatial dissimilarity matrices (i.e., $\underline{\alpha}^*|\alpha_P = 0$), the corresponding convex combination of dissimilarity matrices (i.e., $D_{-P}(\underline{\alpha}^*|\alpha_P = 0)$) will explain as much as possible the dissimilarities in non-spatial matrices, thus being $Q_{D_{-P}}(\mathcal{P}_K^{\underline{\alpha}^*|\alpha_P=0})$ greater than any other potential $Q_{D_{-P}}(\mathcal{P}_K)$ evaluated at $\underline{\alpha}|\alpha_P = 0$. Considering a generic combination of $\underline{\alpha}$ and K , the multi-matrix Joint Inertia for the spatial dissimilarity matrix D_P can be computed as

$$JI_P(\mathcal{P}_K^\alpha) = \tilde{Q}_{D_P}(\mathcal{P}_K^\alpha) - (1 - \tilde{Q}_{D_{-P}}(\mathcal{P}_K^\alpha)) = \frac{Q_{D_P}(\mathcal{P}_K^\alpha)}{Q_{D_P}(\mathcal{P}_K^{\alpha_P=1})} + \frac{Q_{D_{-P}}(\mathcal{P}_K^\alpha)}{Q_{D_{-P}}(\mathcal{P}_K^{\underline{\alpha}^*|\alpha_P=0})} - 1$$

where $\tilde{Q}_{D_{-P}}(\mathcal{P}_K^\alpha)$ is the normalized proportion of explained inertia with respect to the optimal non-spatial setting and $\tilde{Q}_{D_P}(\mathcal{P}_K^\alpha)$ is the normalized proportion of explained inertia with respect to the purely-spatial setting.

As the normalized proportion of explained inertia for every dissimilarity matrix varies between 0 and 1, also the Joint Inertia $JI_P(\mathcal{P}_K^\alpha)$ will range from 0 to 1 (i.e., $0 \leq JI_P(\mathcal{P}_K^\alpha) \leq 1$), being close to zero when the loss in the normalized proportion of explained inertia from the features dissimilarity

due to the inclusion of the spatial component is similar to the normalized proportion of explained inertia in the spatial dissimilarity in the combined partition. Conversely, it will be close to 1 when the clustering partition obtained combining features and spatial dissimilarities allows to explain a high normalized proportion of inertia, both in spatial and non-spatial dissimilarity matrices.

We stress that the Joint Inertia can be utilized to evaluate the contribution of any dissimilarity matrix relative to all other dissimilarity matrices. In this study the Joint Inertia is specifically introduced to assess the role of the spatial component, addressing our initial research objectives. However, in other contexts, the Joint Inertia of any dissimilarity matrix can be computed to gain a comprehensive understanding of which variables exhibit shared explanatory power in terms of their dissimilarities. Further technical details about the Join Inertia, both in the case of two matrices and when considering more than two matrices, are discussed in the Appendix A.

Considering the three simulated scenarios described above, in Table 1 we provide the values of the normalized proportion of explained inertia in D_0 and D_1 and the Joint Inertia obtained for every case represented in Figure 1. When the spatial component is not related to the clustering partition obtained by features (e.g., scenario b), we obtain α being either 0 or 1. Thus, the normalized proportion of explained inertia in the features dissimilarity matrix (or in the spatial dissimilarity matrix) will be equal to 1, while the normalized proportion of explained inertia in the spatial dissimilarity matrix (in the feature dissimilarity matrix) will be close to zero but strictly positive. The Joint Inertia index will be close to zero in cases (a) and (b), which is coherent with the fact that the spatial component plays no role in identifying the actual clustering patterns (conversely, well identified by the features space), while it is equal to 1 in case (c) because the spatial information is strongly related to the underlying phenomenon and exactly describes the groups structure³. When $0 < \alpha < 1$, the dissimilarity matrices are combined because their combination allows us to capture an overall higher proportion of the explained inertia, thus we expect to obtain an higher value of the presented indicator. In the following Section 4 we discuss the connection between the Join Inertia and the spatial information embedded in the data. In particular, we focus on how the index can be used to assess the actual relevance of the geographical dissimilarity in computing the clustering partitions.

³It should be noted that the case $JJ = 1$ holds when the geographical information and the feature space describe the same group structure while being strongly related to the phenomenon under study. This happens when space and features embed the same amount of information associated with the phenomenon and resulting in the same clustering partition. So, in a sense, the geography jointly determines the features and the clusters. However, geography compresses the relevant information using only two dimensions, whereas it is reasonable to expect the same degree of information to be achieved by a much larger number of features.

Case (a)	Case (b)		Case (c)
Spatial component is not relevant	Spatial component is relevant but not related to the features		Spatial component is helpful
$\alpha = 0$ $\tilde{Q}_{D_1}(\mathcal{P}_K^\alpha) \approx 0$ $\tilde{Q}_{D_0}(\mathcal{P}_K^\alpha) = 1$ $JI \approx 0$	if $\alpha = 0$ $\tilde{Q}_{D_1}(\mathcal{P}_K^\alpha) \approx 0$ $\tilde{Q}_{D_0}(\mathcal{P}_K^\alpha) = 1$ $JI \approx 0$	if $\alpha = 1$ $\tilde{Q}_{D_1}(\mathcal{P}_K^\alpha) = 1$ $\tilde{Q}_{D_0}(\mathcal{P}_K^\alpha) \approx 0$ $JI \approx 0$	$0 < \alpha < 1$ $\tilde{Q}_{D_1}(\mathcal{P}_K^\alpha) = 1$ $\tilde{Q}_{D_0}(\mathcal{P}_K^\alpha) = 1$ $JI = 1$

Table 1: Choice of α , normalized proportion of explained inertia and resulting Joint Inertia in different examples of clusters under different spatial conditions. Cases are represented in Figure 1.

4 Simulation experiment

In this section, we provide a simulation experiment aiming to compare the performance of the clustering algorithm based on both [Morelli et al \(2025\)](#) and [Chavent et al \(2018\)](#) variants in choosing the mixing parameter α when considering several settings for the actual contribution of the geographical information. In particular, we provide insights into the role of the spatial component by using an overlapping parameter that controls the distance across the means of the spatial distribution of the true clusters. Under the simulation design, we compare the algorithms in terms of accuracy, precision, sensitivity ([Naidu et al, 2023](#)), and the adjusted rand index ([Gordon, 1999](#)) for multi-class data.

Using a Monte Carlo simulation scheme with $N = 500$ repetitions, we simulate samples of size $n = 100$ observations from a mixture of three-dimensional Gaussian distribution in which the first dimension refers to a unique non-spatial feature and the other two dimensions refer to the spatial coordinates. We simulate data clustered into $K = 4$ different groups. We indicate with π_1, \dots, π_k the probability to sample an observation belonging to each cluster $k = 1, \dots, 4$ and, according to the cluster, we simulate the variable Z and the spatial coordinates (X, Y) . Specifically, we define the distribution of the variable as $Z_k \sim N(\mu_k, \sigma)$, where $\mu_k = (\mu_1, \dots, \mu_4)$ and $\sigma = v$, and the spatial component $(X, Y)_k \sim N(\mu_{sp,k}, \Sigma_{sp})$. The means of the group-specific spatial coordinates are defined according to an overlapping parameter, namely d , which can vary between 0 and 1, and it determines the proximity across the spatial means of the clusters. In particular, $\mu_{sp,k} = (\mu_{sp,1}, \mu_{sp,2}, \mu_{sp,3}, \mu_{sp,4}) = ((d, d), (-d, d), (d, -d), (-d, -d))$ while $\Sigma_{sp} = v_{sp} \mathbb{I}_2$. Notice that, given this simulation setting, as the overlapping parameter grows from 0 to 1, the centroids of the groups tend to diverge, thus generating well-distanced clusters and enhancing the relevance of the geographical information in clustering the units.

To exemplify the contribution of the overlapping parameter d , in Figure 2, we depict some examples of the clustering partition that can be obtained for different values of the overlapping

parameter and distinguishing among [Chavent et al \(2018\)](#) (left column) and [Morelli et al \(2025\)](#) (right column) criteria. The plots are simulated by setting $\pi_k = 1/K$, $\mu_k = (2, 4, 6, 8)$, $v = 0.4$, $v_{sp} = 0.4$, and considering the following set of values for the overlapping parameter $d \in \{0, 1/3, 2/3, 1\}$ (i.e., sorted top-down).

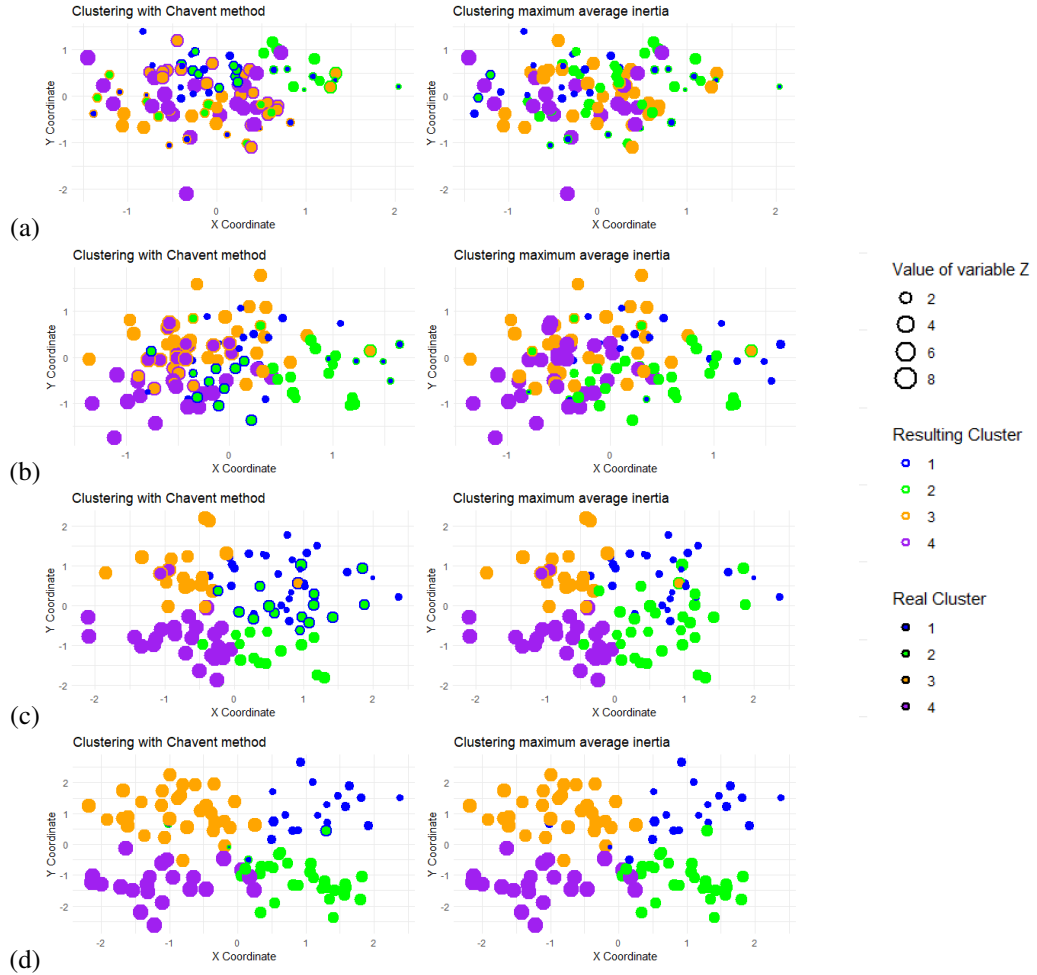


Fig. 2: Clustering partition in four simulations with different overlapping parameters $d \in \{0, 1/3, 2/3, 1\}$ respectively in panel (a), (b), (c), and (d). The color of the points refers to the true cluster from which the observation is drawn, while the color of the border refers to the resulting clustering partition obtained by applying the algorithm from [Chavent et al \(2018\)](#) (left column) and our methodology from [Morelli et al \(2025\)](#) (right column).

From the figure, it is possible to observe that the maximum average criterion is able to detect a clustering partition similar to the real one, even when the spatial component is not relevant or less relevant, that is, in panel *a* and *b*. When the distance in the spatial location of the cluster is higher

(e.g., in panel *c* and *d*), clustering performance improves using both methodologies. Results reported in Table 2 confirm the previous statements. Indeed, while Chavent et al (2018) methodology allows identifying a reasonable clustering partition, the Morelli et al (2025) methodology demonstrates improved clustering performance in terms of accuracy and adjusted rand index. This enhancement is particularly notable in scenarios where the spatial component plays a limited role, such as when clusters fully or partially overlap in space.

d	Chavent et al (2018)			Morelli et al (2025)			Joint Inertia
	α	Accuracy	Adj. RI	α	Accuracy	Adj. RI	
0	0.75	0.43	0.27	0.35	0.87	0.74	0.17
1/3	0.65	0.63	0.34	0.50	0.93	0.83	0.49
2/3	0.85	0.82	0.61	0.45	0.97	0.93	0.86
1	0.75	0.96	0.91	0	1.00	1.00	0.93

Table 2: Comparison of the performance resulting from clustering partition according to Chavent et al (2018) and Morelli et al (2025) algorithm and the resulting Joint Inertia to assess the role of the spatial component in the partition.

Moreover, we confirm that the parameter α can not be interpreted as a measure of assessment of the role of the spatial component as the optimized values do not reflect the degree of overlapping of the data-generating process. On the other hand, the Joint Inertia index appears effective in assessing the relevance of the spatial component in the resulting cluster distribution.

Below, we present the results from the Monte Carlo experiment and random assignment for parameters $\pi_k \sim U(0.15, 0.35)$, $v \sim U(0.1, 0.6)$, $v_{sp} = 0.4$ and $d \sim U(0, 1)$. From Table 3, we can clearly observe that maximum average criterion by Morelli et al (2025) is able to find clustering partitions that are very similar to the true partitions and performs remarkably better in identifying the actual mixing parameter α with respect to the Chavent et al (2018) criterion.

	Accuracy		Precision		Sensitivity		Adj. Rand Index	
	Chavent	Morelli	Chavent	Morelli	Chavent	Morelli	Chavent	Morelli
Mean	0.74	0.85	0.75	0.85	0.74	0.84	0.55	0.71
Median	0.76	0.91	0.78	0.91	0.76	0.90	0.52	0.77
sd	0.16	0.14	0.17	0.15	0.16	0.15	0.23	0.22

Table 3: Comparison of the performance resulting from clustering partition according to Chavent et al (2018) and Morelli et al (2025) algorithm in Monte Carlo simulation, in terms of Accuracy, Precision, Sensitivity ad Adjusted Rand Index.

In Figure 3 we provide a comparison of the resulting clustering performance with respect to the overlapping parameter d used in the simulation. It is evident that Morelli et al (2025) algorithm

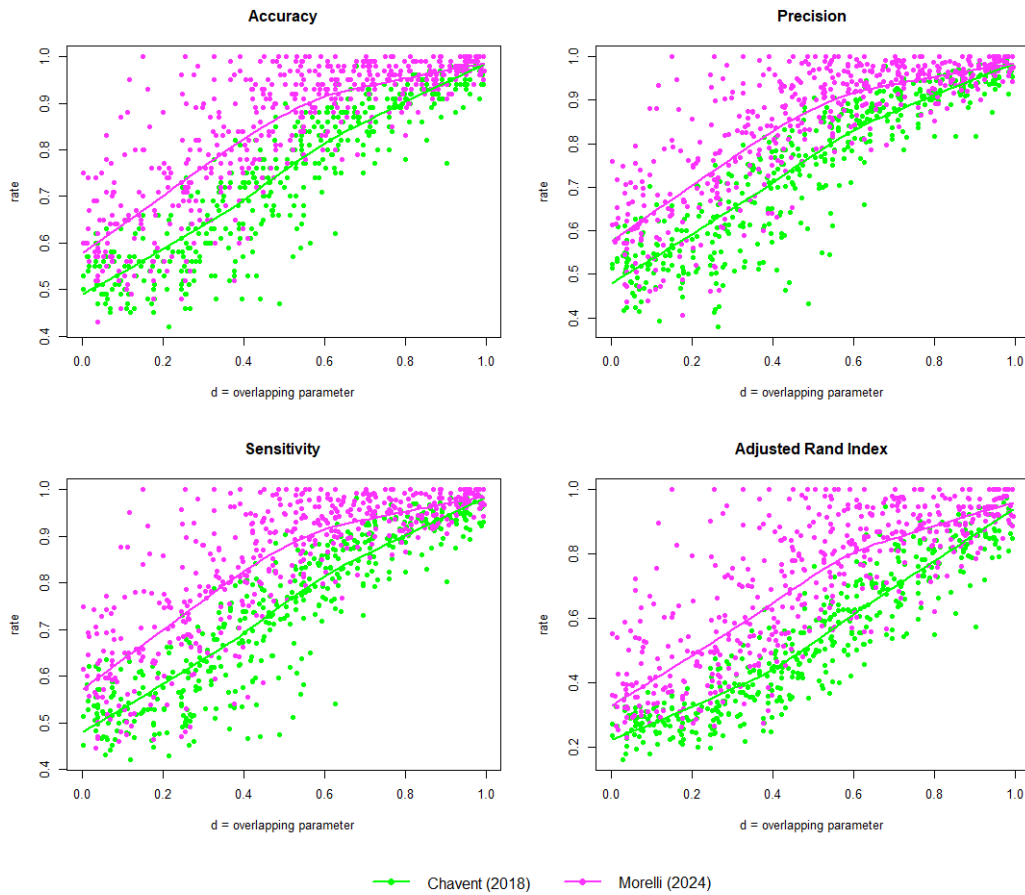


Fig. 3: Clustering performance comparison between [Chavent et al \(2018\)](#) and [Morelli et al \(2025\)](#) in terms of Accuracy, Sensitivity, Precision, and Adjusted Rand Index, with respect to the overlapping parameter d .

performs generally better, in particular when the overlapping parameter is low when clusters are partially overlapping in space. As expected, when the overlapping parameter d is close to 1, both algorithms are able to find exactly the true partition because, as explained in the previous section, when the feature dissimilarity and the spatial dissimilarity lead to the same partition, any combination of them will lead to it.

In Figure 4, we provide several insights into the relationship between the spatial distance among centroids, determined by the overlapping parameter d , the mixing parameter α , and the Joint Inertia index. In the left panel, as the overlapping parameter grows (from left to right), the mixing parameter selected by both methods seems to be unaffected, confirming that the weight assigned to the spatial

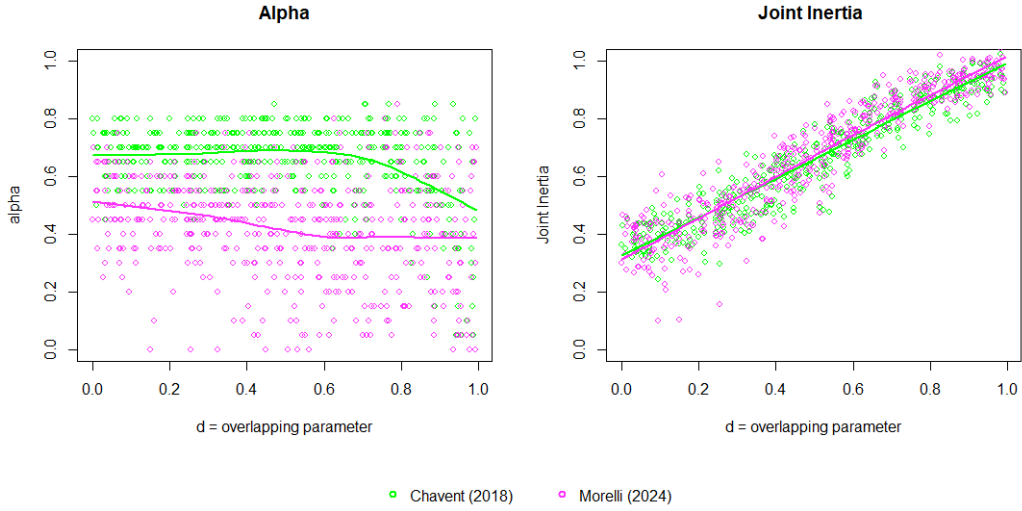


Fig. 4: In panel (a), on the left, we can observe the resulting α according to Chavent et al (2018) and Morelli et al (2025) when considering clusters with different overlapping degrees (i.e., when the overlapping parameter d varies between 0 and 1). In panel (b), on the right, we report the resulting Joint Inertia obtained in the simulation experiment with respect to the overlapping parameter d .

dissimilarity matrix does not provide information about the actual contribution of the spatial component in determining the clusters. Conversely, the right panel remarkably supports the use of the Joint Inertia index in quantifying the importance of the spatial component. Indeed, a strong and positive correlation between the overlapping parameter d and the Joint Inertia is detected, both using $\alpha_{chavent}$ and $\alpha_{morelli}$. The positive correlation is definitely consistent with the interpretation of the overlapping parameter d given above, that is, as d grows from 0 to 1, the distance between the centroids of the groups tends to increase, increasing the informative power induced by the spatial/geographical compared to the non-spatial distance, exactly as described by the Joint Inertia.

5 Dynamic and Regional Clustering of GHGs Emissions

In this section, we present an application of spatiotemporal clustering on environmental data concerning the annual GHGs emissions at the regional level for Europe. Our aim is to explore regional patterns in the environmental impact caused by human activities on air quality, which may also depend on the geographical and morphological characteristics of the area as well as on the productive specialization of the regions.

We analyze the annual average emissions per km² of several GHGs, that is, methane, nitrous oxide, fluorinated gases (F-gases), and carbon dioxide produced by the main economic sectors, namely agriculture, buildings, energy, industry, transport, and waste. Data are measured in tons per km² of CO₂ equivalent.

Greenhouse gases in Europe originate from different activities, each of them contributing to climate change in unique ways (Crippa et al, 2024). Methane (CH₄) emissions primarily arise from agriculture, especially livestock farming and waste management, as well as fossil fuel extraction and processing. Nitrous oxide (N₂O) is largely emitted through agricultural practices, such as the use of nitrogen-based fertilizers, with smaller contributions from industrial processes and fossil fuel combustion. F-gases, synthetic in nature, are used in refrigeration, air conditioning, and industrial processes like aluminum production. Carbon dioxide (CO₂), the most abundant GHGs, is predominantly released through fossil fuel combustion for energy, transportation, and industrial activities, as well as deforestation and cement production.

We believe that the identification of patterns and dynamics in regional GHGs emissions within a spatiotemporal framework is a valuable contribution that extends the current knowledge on the status of environmental degradation in Europe, enhancing the awareness of citizens and institutions regarding the policies to be planned to contrast climate change and global warming.

5.1 Dataset description

The data of interest relate to atmospheric emissions of sector-specific greenhouse gases measured at the regional level provided by the Emissions Database for Global Atmospheric Research (EDGAR) database (Crippa et al, 2024) within the Annual Regional Database of the European Commission (ARDECO) (Bucciarelli, 2024) project. In particular, we consider yearly measurements of GHGs emissions from 1990 to 2022 (i.e., $T = 33$ time stamps) for the $N = 234$ regions⁴ in the European Union, in 27 countries, identified according to the Nomenclature of territorial units for statistics - Level 2 (NUTS-2) classification (European Commission, 2016). We also collect the area of NUTS-2 regions in 2022 from Eurostat ⁵ dataset in order to obtain the annual emissions in tons per km² of CO₂ equivalent, by gases and by sector. In Figure 5 we represent a map of the total GHGs emissions per km² in 2022 at the regional level.

⁴Notice that we excluded regions classified as extra-continental territories and those located in non-European continents, ensuring that the extremely high distances involving these regions do not render the spatial dissimilarities among the remaining regions insignificant.

⁵https://ec.europa.eu/eurostat/databrowser/view/REG_AREA3/default/table

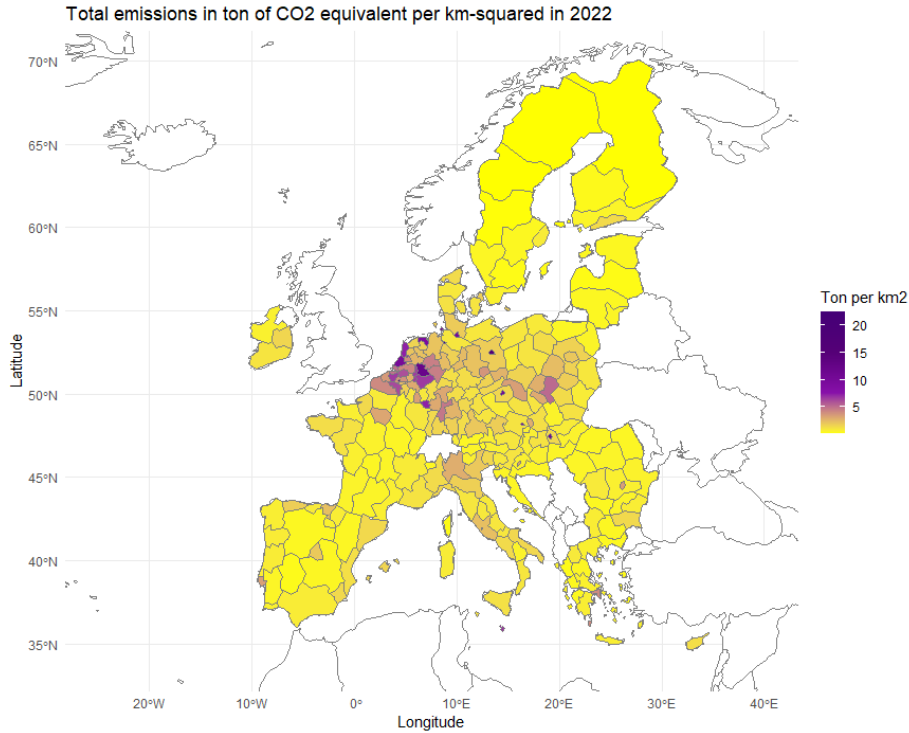


Fig. 5: Map of total emission per km² in 2022 in each region at NUTS2 level.

We run the spatiotemporal cluster analysis twice, considering two different datasets. In the first case, we implement the clustering by aggregating GHGs emissions according to the type of gas (i.e., by summing the emissions at the sectoral level for each gas). In the second case, we aggregate the emissions with respect to the sectors, thus by summing the gas-specific emissions for each sector. In both cases, we utilize the Dynamic Time Warping (DTW) strategy as the chosen distance metric. The Dynamic Programming approach using a warping function has been introduced by [Sakoe and Chiba \(1971, 1978\)](#) in the spoken word recognition field as a time-normalization algorithm. [Berndt and Clifford \(1994\)](#) have implemented DTW distance to detect patterns in time series. We compute the spatial dissimilarity matrix as the geodetic distance across the coordinates of the centroids of each region.

5.2 Spatiotemporal clusters for emissions by gas

We run the algorithm described in [Morelli et al \(2025\)](#) setting $\Delta\alpha = 0.05$, for $K = 2, \dots, 10$, combining $P = 5$ dissimilarity matrices referring to the CH_4 , F-Gases, Fossil- CO_2 , N_2O emission time series and the spatial component. We select $K^* = 4$ according to the elbow rule, observing the

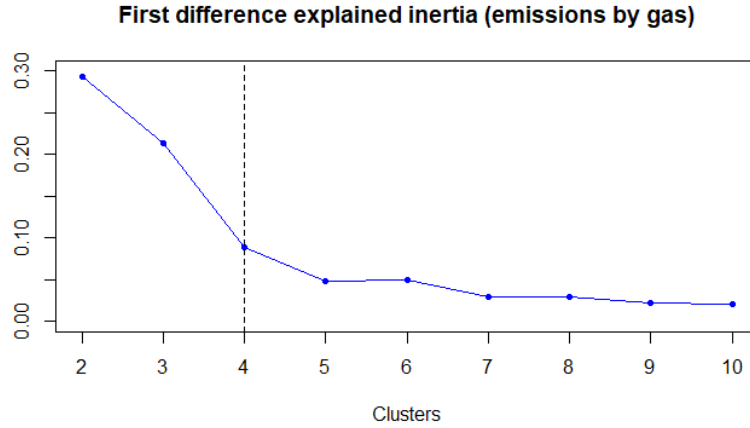


Fig. 6: Increment in the weighted average proportion of explained inertia generated by a unitary increase in the number of clusters. Recall that, for each K , we considered the best combination of the dissimilarity matrices according to the α_K^* found using the maximization inertia criterion.

weighted average proportion of explained inertia, which can be interpreted as the gain in explained variability due to an additional cluster. In Figure 6 we represent the first difference in the weighted average proportion of explained inertia, highlighting our choice of $K^* = 4$.

Consequently, we selected $\alpha_{4,p}^* = (0.20, 0.15, 0.10, 0.20, 0.35)$ as the optimal weighting vector for the dissimilarity matrices. Table 4 provides a summary of the weights α_p^* , the explained inertia (both proportion and normalized), and the Joint Inertia associated with the resulting clustering partition for each dissimilarity matrix included in the algorithm.

From Table 4, it is possible to observe that the partition obtained with $K^* = 4$ clusters allows us to explain almost 40% of the DTW dissimilarities across CO_2 time series and about 60% of the dissimilarities across time series of CH_4 , F-gases, N_2O and the spatial dissimilarity. The latter has a Joint Inertia of 0.55, which allows us to conclude that spatial information is crucial when determining the clusters composition, and therefore, the spatial distance is useful in the identification of patterns to explain well the data under consideration. In particular, through the resulting clustering partition $\mathcal{P}_K^{\alpha^*}$ we are able to incorporate 80% of the explained inertia in the spatial component, relative to the case in which we consider only D_{sp} and, considering the non-spatial dissimilarities, we are still able to include 75% of the explained inertia with respect to the partition obtained excluding the spatial component. All the dissimilarity matrices have a weight greater than zero and they all seem to be relevant in the composition of the clusters, in fact they have a rather high Joint Inertia. it is possible to

note that the weights assigned to the dissimilarity matrices do not always reflect the relevance of the matrix itself in relation to the clustering partition obtained, for example the matrix D_{CO_2} is assigned a weight of 0.2, greater than the 0.15 and 0.10 weights assigned to matrices $D_{F\text{-gases}}$ and D_{N_2O} , yet the proportion of inertia explained in the first, which is 0.38, is less than the inertia explained in the other two, respectively 0.68 and 0.62.

	D_{CH_4}	$D_{F\text{-gases}}$	D_{N_2O}	D_{CO_2}	D_{SP}
α_p^*	0.20	0.15	0.10	0.20	0.35
$Q_{D_p}(\mathcal{P}_K^\alpha)$	0.67	0.68	0.62	0.38	0.58
$\tilde{Q}_{D_p}(\mathcal{P}_K^\alpha)$	0.75	0.82	0.66	0.46	0.80
$\tilde{Q}_{D_{-p}}(\mathcal{P}_K^\alpha)$	0.94	0.93	1.03	0.94	0.75
$JI_p(\mathcal{P}_K^{\alpha^*})$	0.69	0.75	0.68	0.41	0.55

Table 4: Summary of the α^* weights and the inertia (proportion and normalized) returned by the spatiotemporal clustering of emissions by gases at the optimal solution $K^* = 4$. $Q_{D_p}(\mathcal{P}_K^\alpha)$ is the proportion of explained inertia in D_p ; $\tilde{Q}_{D_p}(\mathcal{P}_K^\alpha)$ is the normalized proportion of inertia in D_p ; $\tilde{Q}_{D_{-p}}(\mathcal{P}_K^\alpha)$ is the normalized proportion of inertia excluding D_p ; and $JI_p(\mathcal{P}_K^{\alpha^*})$ is the Joint Inertia relative to D_p .

In Figure 7 we present a map of the regions belonging to different clusters and in Figure 8 we report the average annual emission in each cluster by gas.

Cluster 1 includes regions located in East Europe, from the Scandinavian peninsula to the Balkan countries, the central and southern areas of Italy and the eastern area of Austria. It shows the lowest level of CH_4 , F-gases, CO_2 and N_2O emissions compared to the other clusters and it appears to be quite stable over time, except for F-gases emissions that are slowly increasing.

Regions of the Netherlands, Malta, and several metropolitan areas in East-Central Europe belong to Cluster 2, which is characterized by emission levels that are remarkably higher—by a significant margin—than those observed in any other cluster. As for the dynamics of CH_4 emissions, these exhibit a decreasing trend, nearly halving between 1990 and 2022. Similarly, CO_2 emissions show a decline over the years, dropping from approximately 12 tons per km^2 to about 8 tons per km^2 . In contrast, emissions of F-gases experience a sharp increase during the 1990s, stabilizing thereafter at a level of approximately 0.25 tons per km^2 . Meanwhile, emissions of NO_2 display fluctuations over time without any discernible trend.

Moving to Cluster 3, we can see from the map that it incorporates regions from North-central Europe, mainly Denmark, Germany, east part of France, and Northern Italy. It appears to be the second

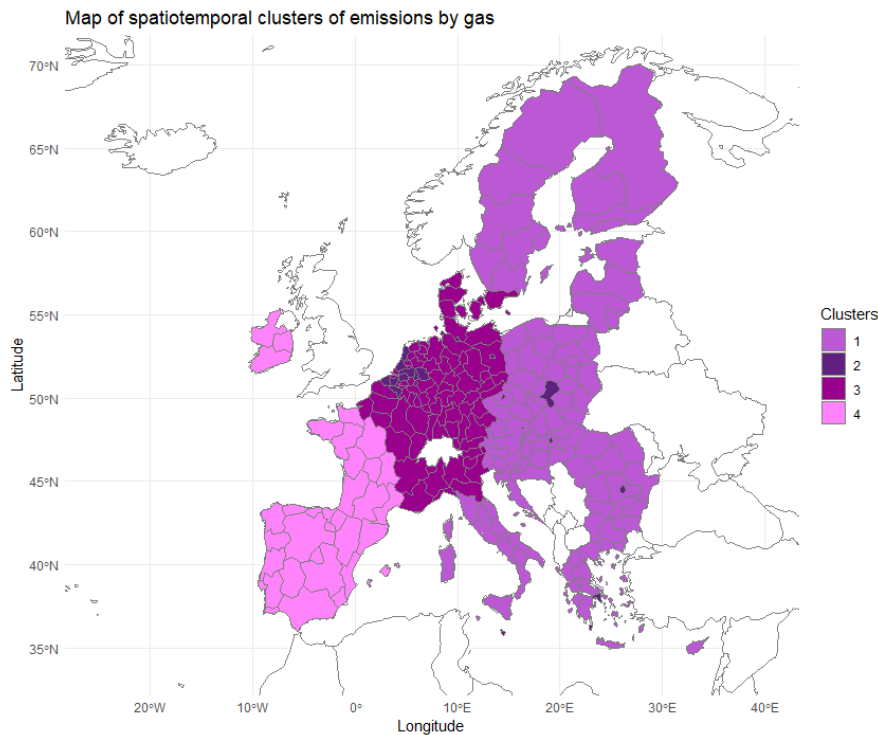


Fig. 7: Map of spatiotemporal clusters obtained combining the dissimilarity matrices of the time series of emissions of different gases between 1990 and 2022, and the geodetic distances across centroids of NUTS2 level regions.

worst cluster in term of emission per km^2 , showing a slowly decreasing trend in CH_4 emissions, quite stable level of CO_2 and F-gases emissions and a drop in NO_2 emissions in the last '90s.

Finally, cluster 4 consists of regions from Ireland, Spain, Portugal, and the West part of France. Regions in this cluster exhibit very low levels of emissions, comparable to those in Cluster 1. These emissions are characterized by a slightly increasing trend for F-gases and stable levels for CH_4 , CO_2 , and N_2O .

In order to better examine the role of the spatial component on cluster formation, we performed non-spatial clustering as a robustness check. The clusters exhibit greater overlap compared to the results obtained with spatiotemporal clustering. However, it remains possible to distinguish regions in Central-Northern Europe as those with the highest levels of emissions per km^2 . A full discussion on the two robustness checks and the corresponding results is reported in Appendix B.1.

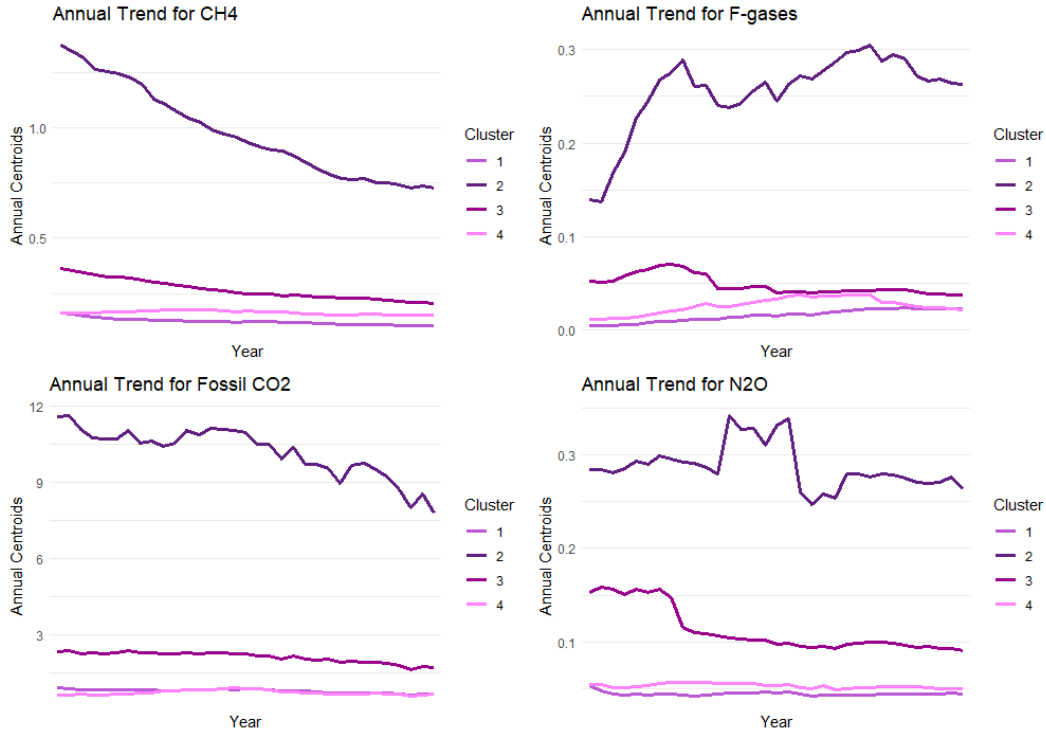


Fig. 8: Annual average of emission per km² of gases for spatiotemporal clusters obtained combining the dissimilarity matrices of the time series of emissions of different gases between 1990 and 2022, and the geodetic distances across centroids of NUTS2 level regions.

5.3 Spatiotemporal clusters for emissions by sector

The second spatiotemporal clustering considers the GHGs emissions by sector. We compute the dissimilarity matrices of the total GHGs emissions in agricultural, buildings, energy, industry, transport, and waste sectors, and we combine them with the spatial dissimilarity matrix, thus having $P = 7$. We set $\Delta\alpha = 0.1$, for $K = 2, \dots, 10$, and we select $K^* = 5$ according to the elbow rule and $\alpha_{5,p}^* = (0.20, 0.10, 0.10, 0.20, 0, 0.10, 0.30)$ as the weight of the dissimilarity matrices. In Figure 9, we represent the first difference in the weighted average proportion of explained inertia, highlighting our choice of $K^* = 5$.

In Table 5, we report a summary of the weights $\underline{\alpha}^*$, the explained inertia (proportion and normalized), and the Joint Inertia in the resulting clustering partition for each dissimilarity matrix included in the algorithm.

From Table 5, it is possible to observe that the partition obtained with $K^* = 5$ clusters allows to explain at least 35% of the proportion of inertia in each dissimilarity matrix and the 36% of the

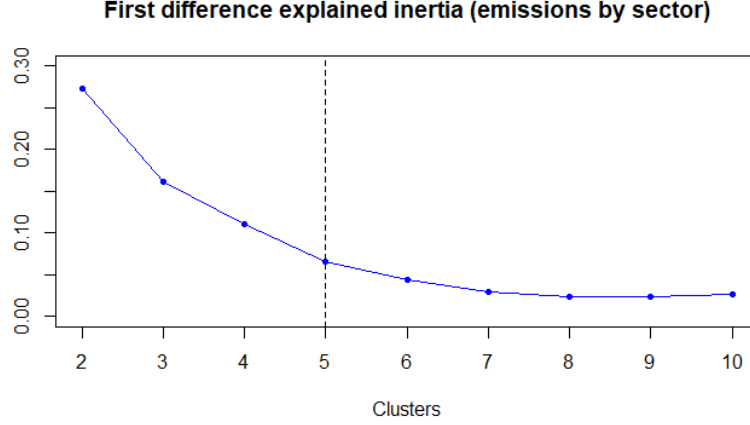


Fig. 9: Increment in the weighted average proportion of explained inertia generated by a unitary increase in the number of clusters. Recall that, for each K , we considered the best combination of the dissimilarity matrices according to the α_K^* found using the maximization inertia criterion.

inertia with respect to the cases in which clusters are computed only relying on one dissimilarity matrix. Each dissimilarity matrix seems to be quite helpful in obtaining the resulting partition. In particular, the spatial component presents a Joint Inertia equal to 0.65, and it incorporates 0.83 of the inertia normalized to the explained inertia in the partition obtained from the purely spatial case. On the other hand, including the spatial component, we are still able to capture 0.73 of the inertia in the non-spatial component. Although all the dissimilarity matrix D_{Tran} has weights equal to 0, thus it is not included in the combined dissimilarity matrix, the resulting partition incorporates 0.61 of the inertia, which corresponds to the 67% normalized to the explained inertia from the partition obtain only considering D_{Tran} .

	D_{Agri}	D_{Build}	D_{Energy}	D_{Ind}	D_{Tran}	D_{Waste}	D_{sp}
α_p^*	0.20	0.10	0.10	0.20	0.00	0.10	0.30
$Q_{D_p}(\mathcal{P}_K^\alpha)$	0.69	0.57	0.35	0.58	0.62	0.61	0.65
$\tilde{Q}_{D_p}(\mathcal{P}_K^\alpha)$	0.72	0.59	0.36	0.60	0.67	0.70	0.83
$\tilde{Q}_{D_{-p}}(\mathcal{P}_K^\alpha)$	0.93	0.99	1.00	0.95	0.99	0.94	0.73
$JI_p(\mathcal{P}_K^{\alpha^*})$	0.65	0.58	0.35	0.55	0.67	0.64	0.56

Table 5: Summary of the α^* weights and the inertia (absolute, relative, and normalized) returned by the spatiotemporal clustering of emissions by gases at the optimal solution $K^* = 4$. $Q_{D_p}(\mathcal{P}_K^\alpha)$ is the proportion of explained inertia in D_p ; $\tilde{Q}_{D_p}(\mathcal{P}_K^\alpha)$ is the normalized proportion of inertia in D_p ; $\tilde{Q}_{D_{-p}}(\mathcal{P}_K^\alpha)$ is the normalized proportion of inertia excluding D_p ; and $JI_p(\mathcal{P}_K^{\alpha^*})$ is the Joint Inertia relative to D_p .

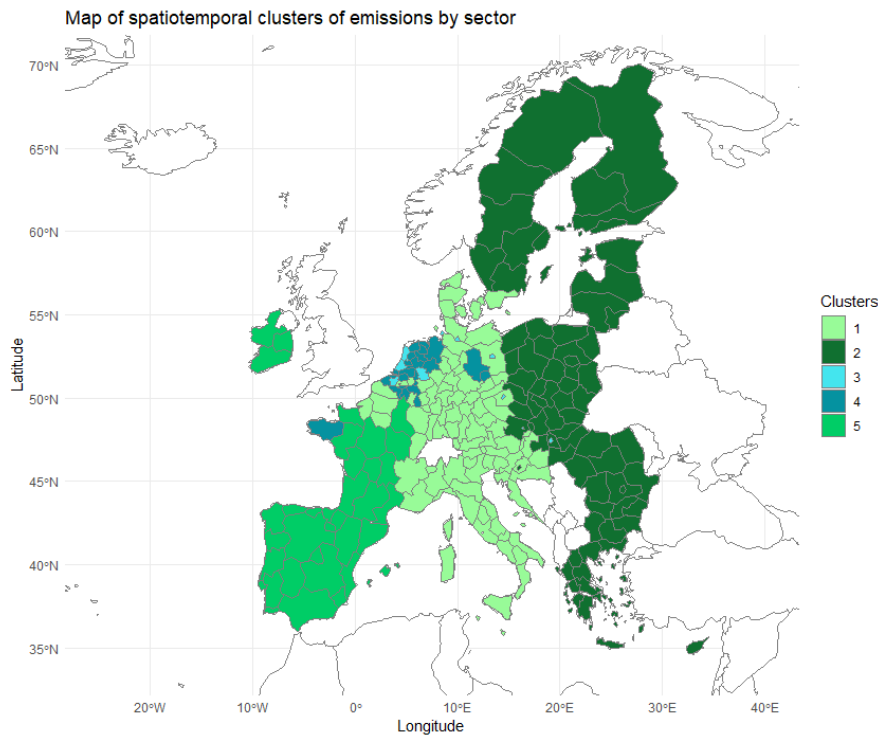


Fig. 10: Map of spatiotemporal clusters obtained combining the dissimilarity matrices of the time series of emissions of different sectors between 1990 and 2022, and the geodetic distances across centroids of nuts2 level regions.

In Figure 10 we present a map of the regions belonging to different clusters and in Figure 11 we report the average annual emission in each cluster, for each sector.

Cluster 1 primarily includes regions located in Central Europe, such as Germany, Denmark, the Czech Republic, Austria, Italy, Croatia, Slovenia, along with a few regions of France. This cluster exhibits steady levels of emissions, which are neither the highest nor the lowest compared to other clusters across all sectors.

Cluster 2 consists primarily of regions in Eastern Europe, including Finland, Sweden, Latvia, Lithuania, Poland, Slovakia, Hungary, Romania, Bulgaria, and Greece. This cluster exhibits the overall lowest emission levels, with stable trends in the Buildings, Energy, Industry, and Waste sectors. Emissions in the Agricultural sector show a slight decrease during the 1990s, while emissions in the Transport sector display a gradual increase over time. Cluster 3 includes the smallest number of regions, located in Belgium and the Netherlands and some metropolitan areas in Germany and Eastern Europe. As highly industrialized and densely populated areas, it is unsurprising that this group exhibits the highest levels of emissions across all sectors except Agriculture. In particular,

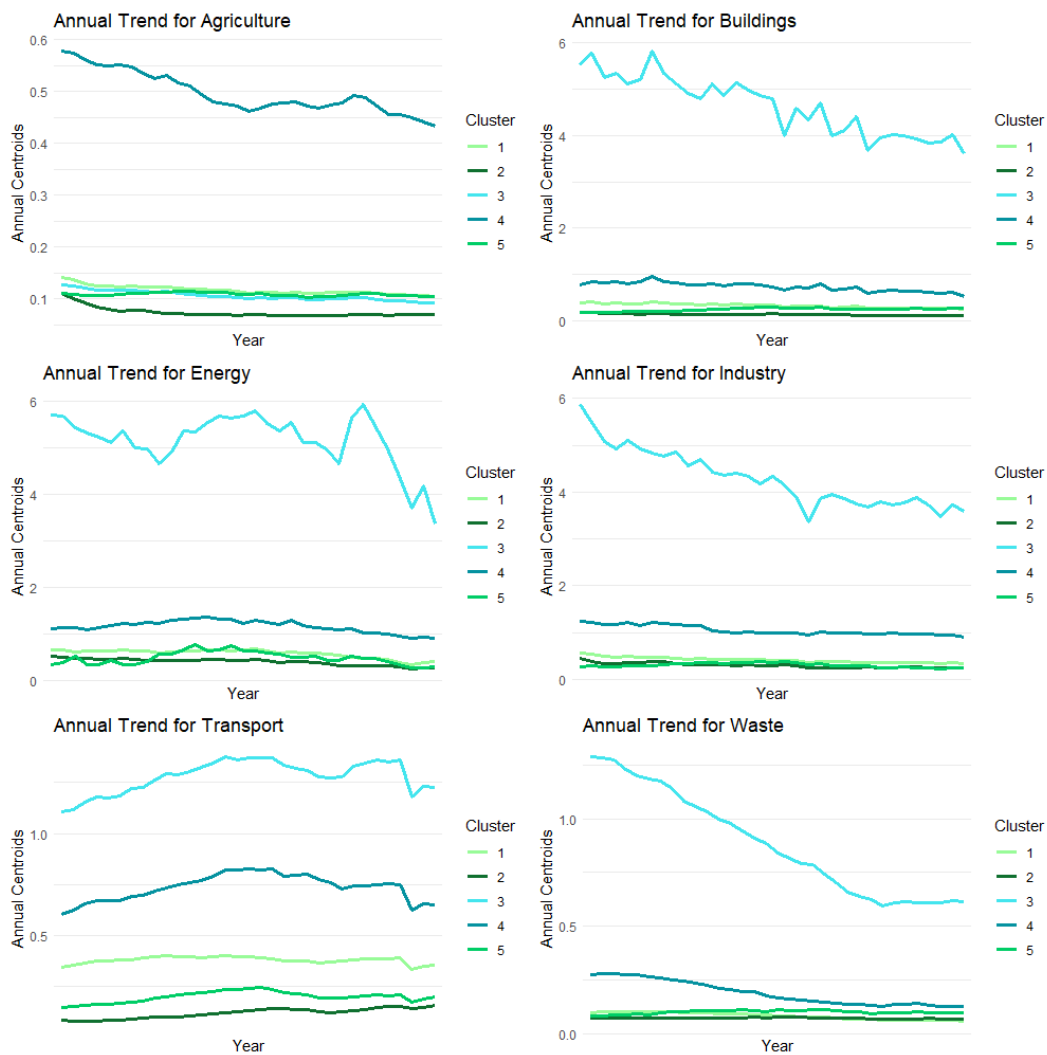


Fig. 11: Annual average of emission per km² of sectors for spatiotemporal clusters obtained combining the dissimilarity matrices of the time series of emissions of different sectors between 1990 and 2022, and the geodetic distances across centroids of nuts2 level regions.

emissions from the Buildings and Industry sectors display a decreasing trend, declining from 6 tonnes per km² to less than 4 tonnes per km². Emissions from the Energy sector demonstrate high variability over time, with a clear reduction from 6 to 3.5 tonnes per km² in the last five years. Waste emissions also follow a generally decreasing trend but appear to have stabilized in recent years. Notably, only the Transport sector shows an increase in emissions over time.

Considering Cluster 4, it includes regions located in Belgium and the Netherlands, Northern France and Northern Germany. This group is characterized by particularly high levels of emissions in the Agricultural sector, which exhibit a decreasing trend over time. For other sectors, it ranks as

the second worst cluster, following Cluster 3. In the Transport and Waste sectors, emissions follow a dynamic similar to Cluster 3, showing increasing and decreasing trends, respectively, while no clear trend is observed in the Buildings, Energy, and Industry sectors.

Finally, cluster 5 comprises regions located in Spain, Portugal, Ireland, and certain areas of France. This group is characterized by relatively low emissions across all sectors. Notably, emission levels in this group do not exhibit pronounced rising or falling trends. However, a slight upward trend is observed in the Transport sector, while the Energy sector shows a modest decline over time.

Overall, we can conclude that a relatively small number of regions, encompassing a limited portion of the European territory, are responsible for exceptionally high GHG emissions. Within each breakdown, a group with particularly elevated emission levels could be distinctly identified. While it is clear that this small group contributes disproportionately to total emissions, it is equally evident that these regions also exhibit decreasing trends over time. This suggests ongoing improvements, albeit at varying rates, across individual sectors and for gases with higher emission levels.

To further investigate the role of the spatial component in cluster formation, we performed non-spatial clustering as a robustness check for emissions by sector, similarly to the previous case. The resulting clusters show greater overlap compared to the spatiotemporal clustering approach. Nevertheless, regions in Central-Northern Europe and metropolitan areas remain identifiable as those with the highest levels of emissions per km² across multiple sectors. A detailed discussion of this robustness check and the associated results can be found in [Appendix B.2](#).

6 Conclusion

Spatiotemporal hierarchical clustering methodology is a versatile and flexible approach to analyze patterns and dynamics of complex phenomena. In our study, we applied this methodology to greenhouse gas emissions across European regions, combining temporal emission patterns and spatial proximity into a unified analysis. Notably, we sought to assess whether the geographical information is helpful in explaining emission dynamics, providing both methodological advancements and empirical insights.

To this end, we introduced a novel measure, the Joint Inertia, to evaluate the role of the spatial component in the clustering process. This measure captures the contribution of spatial distances in generating the final clustering partition. Through a simulation experiment, we demonstrated the

advantages of our methodology and highlighted how the Joint Inertia effectively quantifies the influence of spatial information on the clustering results. These findings underscore the robustness of our approach and its capacity to reveal spatial-temporal structures in the data that might otherwise remain hidden.

Our application provides compelling evidence that spatial context meaningfully enhances the analysis of emission trends. The Joint Inertia values indicate that including spatial distances enriches the clustering process, revealing region-specific patterns and dynamics that reflect Europe's inherent heterogeneity in economic, industrial, and social characteristics.

By separately analyzing emissions by gas type and sector, we uncovered distinct trends and dynamics within each cluster. This analysis highlighted how regions with high emissions are often associated with specific sectors, such as agriculture or industry, while others demonstrate relatively low emissions with stable or slowly evolving patterns. The interplay of gas-specific and sector-specific emissions varies significantly across regions, reflecting the diverse economic, industrial, and social landscapes of Europe. This detailed approach provides a more nuanced understanding of emission patterns, identifying both hotspots of high emissions and regions with notable improvements or stability. Such insights are invaluable for tailoring regional environmental policies and strategies to address sector-specific challenges effectively.

The methodological contributions and empirical findings of this study hold significant utility for both statisticians and environmental researchers. From a methodological perspective, our approach demonstrates the versatility of spatiotemporal clustering for high-dimensional data, offering a framework that can be adapted to other environmental and socioeconomic phenomena. For environmental research, this study delivers actionable insights into the spatiotemporal dynamics of greenhouse gas emissions, offering a foundation for targeted mitigation policies and resource allocation.

Future work could extend these contributions by linking cluster dynamics to socioeconomic, industrial, or policy variables, further enriching the understanding of emission drivers, exploiting proper spatiotemporal models. This would enable a more comprehensive framework for analyzing greenhouse gas emissions in a holistic spatiotemporal context, paving the way for interdisciplinary research and evidence-based policy development.

Declarations

- **Funding:** This study was partly funded by the University of Milano-Bicocca in the framework of the Sequestering CARbon through Forests, AgriCulture, and land use (SCARFACE) research project (2024-ATEQC-0048).
- **Conflict of interest and competing interests:** The authors have no competing interests to declare that are relevant to the content of this article.
- **Data and code availability:** Data used in the paper are public (source JRC-ARDECO). Since we use only public data, no Special Permission is need to use copyrighted material from other sources (including the Internet). All results presented in this paper can be reproduced using the R statistical software. The codes were developed entirely by the authors. For reproducibility purposes, we attach to the present submission code and data. After the peer-review process, in the case of a positive outcome, all the scripts and the data are made public through a dedicated GitHub webpage.
- **Declaration of Generative AI and AI-Assisted Technologies in the Writing Process:** During the preparation of this work, the authors used ChatGPT, a generative AI tool developed by OpenAI, to assist with drafting, rephrasing, and refining the text. After utilizing this tool, the authors carefully reviewed, edited, and revised the content as necessary to ensure accuracy, clarity, and alignment with the objectives of the publication. The authors take full responsibility for the content of this manuscript, including any ideas, analyses, and conclusions presented.

Appendix A Technical details of Joint Inertia

In this appendix we focus on the properties of Joint Inertia, in particular we explain why its value varies between 0 and 1 and what are the conditions that guarantee it, starting from the simplest case where we have only two matrices of dissimilarity and then extending the reasoning to the case where we want to combine more than two matrices.

A.1 Joint Inertia for the case $P = 2$ dissimilarity matrices

Let $D_0 = [d_{0,ij}]_{i,j=1,\dots,n}$ and $D_1 = [d_{1,ij}]_{i,j=1,\dots,n}$ refer respectively to any distances matrix of variables and the spatial distances matrix considering a sample of n units. Let us consider a partition \mathcal{P}_K^α in K clusters obtained mixing the dissimilarity matrices D_0 and D_1 with the parameter α . Also, let us denote its within-clusters mixed inertia as $W(\mathcal{P}_K^\alpha)$ and the corresponding proportion of the

total pseudo inertia explained as

$$Q_0(\mathcal{P}_K^\alpha) = 1 - \frac{W_0(\mathcal{P}_K^\alpha)}{W_0(\mathcal{P}_1)} \quad Q_1(\mathcal{P}_K^\alpha) = 1 - \frac{W_1(\mathcal{P}_K^\alpha)}{W_1(\mathcal{P}_1)},$$

where $W_0(\mathcal{P}_1)$ and $W_1(\mathcal{P}_1)$ are the total pseudo inertia under dissimilarity matrix D_0 and under dissimilarity matrix D_1 , respectively. It is easy to observe that the possible values of this ratio vary between 0 and 1 because the sum of the square dissimilarities between the units belonging to the same clusters will not be greater than the total of the square dissimilarities within a matrix, and being quantities square, will all have positive values, for each possible value of α .

The resulting mixed dissimilarity matrix $D = (1-\alpha)D_0 + \alpha D_1$ will reflect more the dissimilarities in D_0 (or D_1), when the value of α is closer to 0 (or close to 1), thus the resulting partition \mathcal{P}_K^α will be able to capture an higher proportion of explained inertia in D_0 (or D_1). Therefore, when α increases, $Q_{D_0}(\mathcal{P}_K^\alpha)$ will increase and $Q_{D_1}(\mathcal{P}_K^\alpha)$ will decrease. This is also explained in details in Section 3.2 of [Chavent et al \(2018\)](#). Notice that the proportion of explained inertia is equal to 0 only when $K = 1$ and it is 1 only when $K = n$, for each value of α . Following we summarize and formalize the concept which hold for $1 < K < n$

$$0 = Q_{D_0}(\mathcal{P}_{K=1}) < Q_{D_0}(\mathcal{P}_K^{\alpha=1}) \leq Q_{D_0}(\mathcal{P}_K^\alpha) \leq Q_{D_0}(\mathcal{P}_K^{\alpha=0}) < Q_{D_0}(\mathcal{P}_{K=n}) = 1$$

$$0 = Q_{D_1}(\mathcal{P}_{K=1}) < Q_{D_1}(\mathcal{P}_K^{\alpha=0}) \leq Q_{D_1}(\mathcal{P}_K^\alpha) \leq Q_{D_1}(\mathcal{P}_K^{\alpha=1}) < Q_{D_1}(\mathcal{P}_{K=n}) = 1.$$

Now, we consider the normalized proportion of explained inertia for dissimilarity matrix D_0 (or D_1), which correspond to the ratio between the proportion of explained inertia in the partition obtained using the combined dissimilarity matrix with parameter α , and the proportion of inertia explained using only the features (or spatial) dissimilarities, thus the maximum proportion of explained inertia.

$$\tilde{Q}_{D_0}(\mathcal{P}_K^\alpha) = \frac{Q_{D_0}(\mathcal{P}_K^\alpha)}{Q_{D_0}(\mathcal{P}_K^0)} \quad \tilde{Q}_{D_1}(\mathcal{P}_K^\alpha) = \frac{Q_{D_1}(\mathcal{P}_K^\alpha)}{Q_{D_1}(\mathcal{P}_K^1)}.$$

These quantities are strictly positive and no greater than 1. In particular, the normalized proportion of explained inertia in D_0 (or D_1) reaches its minimum value when the feature (or spatial) dissimilarity matrix is not included in the combination, thus $\alpha = 1$ (or $\alpha = 0$), and it reaches its

maximum when the clustering partition is obtained from the purely no-spatial (or spatial) case.

$$0 < \tilde{Q}_{D_0}(\mathcal{P}_K^{\alpha=1}) \leq \tilde{Q}_{D_0}(\mathcal{P}_K^\alpha) \leq \tilde{Q}_{D_0}(\mathcal{P}_K^{\alpha=0}) = 1$$

$$0 < \tilde{Q}_{D_1}(\mathcal{P}_K^{\alpha=0}) \leq \tilde{Q}_{D_1}(\mathcal{P}_K^\alpha) \leq \tilde{Q}_{D_1}(\mathcal{P}_K^{\alpha=1}) = 1$$

The Joint Inertia between two dissimilarity matrices is computed using the following formula

$$JI(\mathcal{P}_K^\alpha) = \tilde{Q}_{D_1}(\mathcal{P}_K^\alpha) - (1 - \tilde{Q}_{D_0}(\mathcal{P}_K^\alpha)) = \frac{Q_{D_1}(\mathcal{P}_K^\alpha)}{Q_{D_1}(\mathcal{P}_K^1)} + \frac{Q_{D_0}(\mathcal{P}_K^\alpha)}{Q_{D_0}(\mathcal{P}_K^0)} - 1.$$

It is strictly positive because the partition obtained from the mixed dissimilarity matrix allows at least to explain as much as the partition obtained from purely non-spatial case in D_0 or the partition obtained from purely spatial case in D_1 . This has already been explained extensively in Section 3, through Figure 1 and Table 1.

A.2 Joint Inertia for the case $P > 2$ dissimilarity matrices

The generalization to the case of multiple dissimilarity matrices, one of which relates to the spatial component, is straightforward. Let us suppose that we are interested in computing the Joint Inertia for the generic variable m (with m being the generic index for the P variables of interests) compared to the combination of all the other variables used to cluster the time series ⁶.

Recalling the notation previously introduced, let us consider a set of P variables observed over time at n spatial locations (or regions) and let $\underline{\alpha} = [\alpha_p]_{p=1,2,\dots,P} = (\alpha_1, \alpha_2, \dots, \alpha_p, \dots, \alpha_P)$ be the vector of mixing weights⁷ used to compute the linear combination of all the dissimilarity matrices $D(\underline{\alpha}) = \sum_{p=1}^P \alpha_p D_p$ subject to $\alpha_p > 0 \quad \forall p = 1, \dots, P$ and $\sum_{p=1}^P \alpha_p = 1$.

By applying the Ward-like hierarchical clustering algorithm presented in the manuscript to the matrix $D(\underline{\alpha})$ generated by a given combination of mixing parameters $\underline{\alpha}$ and number of clusters K the resulting partition is denoted as \mathcal{P}_K^α . Given the generic partition \mathcal{P}_K^α obtained from the mixed

⁶In the main manuscript, we focused on the specific case of the Joint Inertia for the spatial dissimilarity matrix, that we assumed to be the P -th variable. Hence, the results in the Appendix can be related to the results in the main manuscript by assuming that $m = P$.

⁷Notice that, although the grid can be either regular or irregular, here we consider a regular grid with constant step $\Delta\alpha$.

dissimilarity matrix, the proportion of explained inertia for matrix m -th is computed as

$$Q_{D_p}(\mathcal{P}_K^\alpha) = 1 - \frac{W_{D_p}(\mathcal{P}_K^\alpha)}{W_{D_p}(\mathcal{P}_1)}$$

and the normalized proportion of explained inertia, with respect to the case in which only variable p is used, is computed as

$$\tilde{Q}_{D_p}(\mathcal{P}_K^\alpha) = \frac{Q_{D_p}(\mathcal{P}_K^\alpha)}{Q_{D_p}(\mathcal{P}_K^{\alpha_p=1})}$$

Recall that these quantities are both included between 0 and 1 for the same reasons and considerations as in the case of two dissimilarity matrices.

To retrieve the equation of the Joint Inertia for variable m we need to focus on two dissimilarity matrices: the first is the matrix related to m -th variable of interest on which to compute the index and the second is the linear combination of all the others dissimilarity matrices different from m (i.e., the complementary matrices). Let $D_m = [d_{m,ij}]_{i,j=1,\dots,n}$ be the dissimilarity matrix for variable m across the n units and let $D_{-m} = [d_{p,ij}]_{p=1,\dots,m-1,m+1,\dots,P; i,j=1,\dots,n}$ be the dissimilarity matrices containing the distances across the $P - 1$ time series different from m . Moreover, let us define the matrix $D_{-m}(\underline{\alpha}|\alpha_m = 0) = \sum_{p \neq m} \alpha_p D_p$ as the combination of the $P - 1$ dissimilarity matrices excluding the m -th dissimilarity matrix D_m , and the resulting clustering partition as $\mathcal{P}_K^{\underline{\alpha}|\alpha_m=0}$. Similarly, define the partition obtained by using only the information contained in the m -th matrix (i.e., by fixing $\alpha_m = 1$) as $\mathcal{P}_K^{\alpha_m=1}$.

If we denote the total inertia in D_{-m} as $W_{D_{-m}}(\mathcal{P}_1)$, we can compute the following quantities

$$Q_{D_{-m}}(\mathcal{P}_K^\alpha) = 1 - \frac{W_{D_{-m}}(\mathcal{P}_K^\alpha)}{W_{D_{-m}}(\mathcal{P}_1)} \quad Q_{D_{-m}}(\mathcal{P}_K^{\underline{\alpha}|\alpha_m=0}) = 1 - \frac{W_{D_{-m}}(\mathcal{P}_K^{\underline{\alpha}|\alpha_m=0})}{W_{D_{-m}}(\mathcal{P}_1)}$$

which represent the proportion of explained inertia induced by the complementary matrices evaluated at the generic vector of mixing parameters $\underline{\alpha}$ (left formula) and the the proportion of explained inertia induced by the complementary matrices evaluated at the restricted vector $\underline{\alpha}|\alpha_m = 0$ which does not consider the m -th matrix⁸ (right formula).

⁸Notice that, when m is the spatial matrix, the first formula corresponds to the proportion of explained inertia induced by the feature combined dissimilarity matrix when including the spatial component, while the second formula is the proportion of explained inertia induced by the feature combined dissimilarity matrix when excluding the spatial component.

The normalized proportion of explained inertia in the non-spatial combined dissimilarity matrix can be computed as

$$\tilde{Q}_{D_{-m}}(\mathcal{P}_K^\alpha) = \frac{Q_{D_{-m}}(\mathcal{P}_K^\alpha)}{Q_{D_{-m}}(\mathcal{P}_K^{\alpha^*|\alpha_m=0})}$$

By definition, all these quantities are bounded between 0 and 1. Indeed, If we employ one of the procedures in [Chavent et al \(2018\)](#) or [Morelli et al \(2025\)](#) to compute the optimal weighting vector for the combination of all the dissimilarity matrices different from m (i.e., $\underline{\alpha}^*|\alpha_m = 0$ subject to $\sum_{p \neq m} \alpha_p = 1$), then, the corresponding convex combination of dissimilarity matrices (i.e., $D_{-m}(\underline{\alpha}^*|\alpha_m = 0)$) will explain as much as possible the dissimilarities in the D_m matrices, thus being $Q_{D_{-m}}(\mathcal{P}_K^{\alpha^*|\alpha_m=0})$ greater than any other potential $Q_{D_{-m}}(\mathcal{P}_K^{\alpha|\alpha_m=0})$.

Finally, considering a generic combination of $\underline{\alpha}$ and K , the Joint Inertia for variable m when the number of dissimilarity matrices is $P > 2$ can be determine by the following formula

$$JI_m(\mathcal{P}_K^\alpha) = \tilde{Q}_{D_m}(\mathcal{P}_K^\alpha) - (1 - \tilde{Q}_{D_{-m}}(\mathcal{P}_K^\alpha)) = \frac{Q_{D_m}(\mathcal{P}_K^\alpha)}{Q_{D_m}(\mathcal{P}_K^{\alpha_m=1})} + \frac{Q_{D_{-m}}(\mathcal{P}_K^\alpha)}{Q_{D_{-m}}(\mathcal{P}_K^{\alpha^*|\alpha_m=0})} - 1.$$

Similarly to the case where we had only two matrices, if the matrix D_m does not play some useful role in identifying groups compared with all other dissimilarity matrices, one of the normalized proportion of explained inertia takes value 1 and the other one will be close to 0 but strictly positive. If the dissimilarity matrix D_m alone and the combined dissimilarity matrix excluding D_m lead exactly to the same partition we would obtain using the combination of all dissimilarity matrices, thus $\mathcal{P}_K^{\alpha_m=1} = \mathcal{P}_K^{\alpha^*|\alpha_m=0} = \mathcal{P}_K^\alpha$ the resulting Joint Inertia is exactly 1, thus its maximum value, reflecting the crucial role of matrix D_m which is able to perfectly explain the same sum of square dissimilarity of the other variables, even if they are not included.

Appendix B Non-spatial clustering

With the aim of better illustrating the utility of the spatiotemporal clustering methodology employed and emphasizing the role of the spatial component—central to this paper—in this appendix, we present the results obtained from performing the cluster analysis without incorporating the spatial component. This comparison underscores the added value of integrating spatial information in identifying meaningful patterns and dynamics in the data.

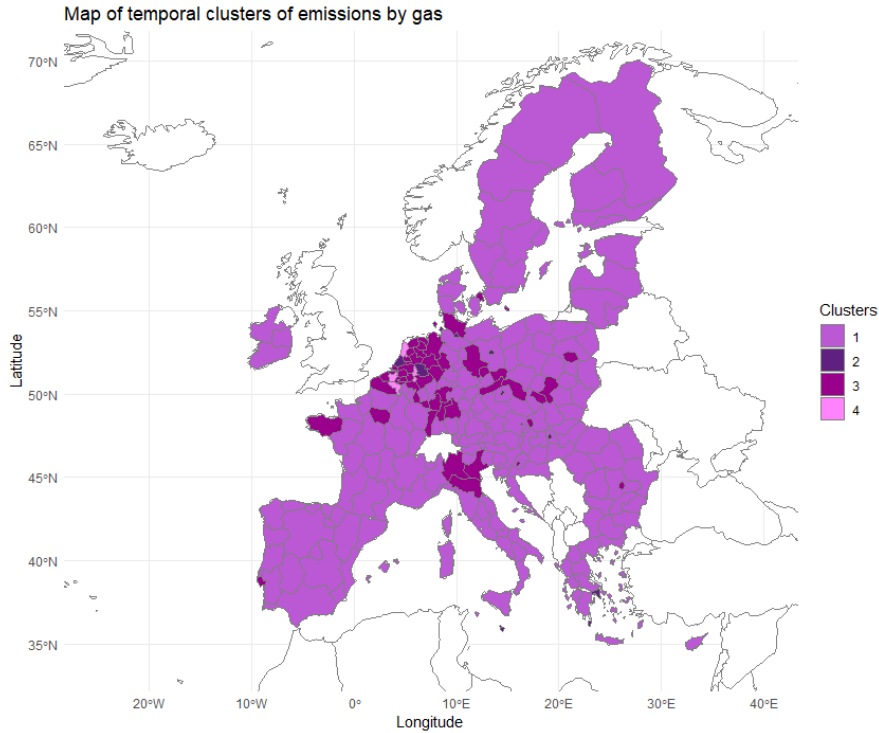


Fig. B1: Map of temporal clusters obtained combining the dissimilarity matrices of the time series of emissions of different gases between 1990 and 2022.

B.1 Temporal clustering for emissions by gas

Considering dissimilarity matrices D_{CH_4} , $D_{F-gases}$, D_{N_2O} and D_{CO_2} , as defined in Section 5.2, we set $\Delta\alpha = 0.05$ and $K = 4$ and we obtain $\alpha_{4,p}^* = (0.1, 0.35, 0.15, 0.4)$ as the optimal weighting vector for the dissimilarity matrices. In Figure B1 we show a map of the regions belonging to different clusters and in Figure B2 we provide the average annual emission in each cluster by gas.

The clustering results exhibit a high degree of spatial overlap, yet discernible spatial patterns remain evident. Notably, regions in clusters 1 and 2, which demonstrate the poorest performance, include Belgium, the Netherlands, and certain metropolitan areas in Northern Europe. These regions display a decreasing trend in emissions for the gases with the highest levels, namely CH_4 and CO_2 . In contrast, cluster 3 consists of sparsely populated regions in Central Europe with significantly lower emissions than the previous clusters. Lastly, the cluster encompassing the largest number of regions, covering over two-thirds of the analyzed area, is characterized by remarkably low emissions and appears relatively stable over time.

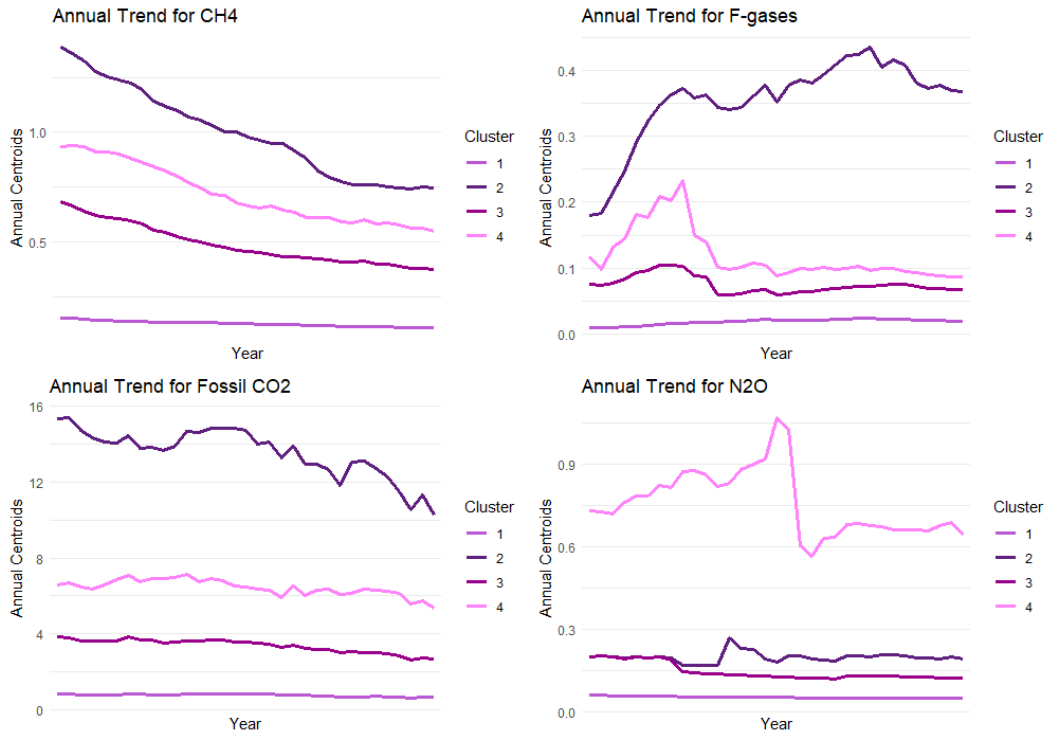


Fig. B2: Annual average of emission per km² of sectors for temporal clusters obtained combining the dissimilarity matrices of the time series of emissions of different gases between 1990 and 2022.

B.2 Temporal clustering for emissions by sector

Moving to the emissions by sectors, we consider dissimilarity matrices D_{Agri} , D_{Build} , D_{Energy} , D_{Ind} , D_{Tran} and D_{Waste} , as defined in Section 5.3, we set $\Delta\alpha = 0.1$ and $K = 5$ and we obtain $\alpha_{5,p}^* = (0.3, 0, 0.2, 0, 0.3, 0.2)$ as the optimal weighting vector for the dissimilarity matrices. In Figure B3 we provide a map of the regions belonging to different clusters and in Figure B4 we describe the average annual emission in each cluster by gas.

From the results, we can immediately see that, even without incorporating the spatial component, there is still a degree of spatial overlap in the clustering outcomes. Notably, regions with particularly low performance are concentrated within the European Union. Specifically, Cluster 1, the largest in terms of geographic area, exhibits very low emission levels across all sectors, with no discernible increasing or decreasing trends. Cluster 2 encompasses industrial regions in Northern Europe, characterized by high emissions in the Energy and Industry sectors, which show a declining trend over time. Cluster 3 is associated with low, though not minimal, emission levels, accompanied by

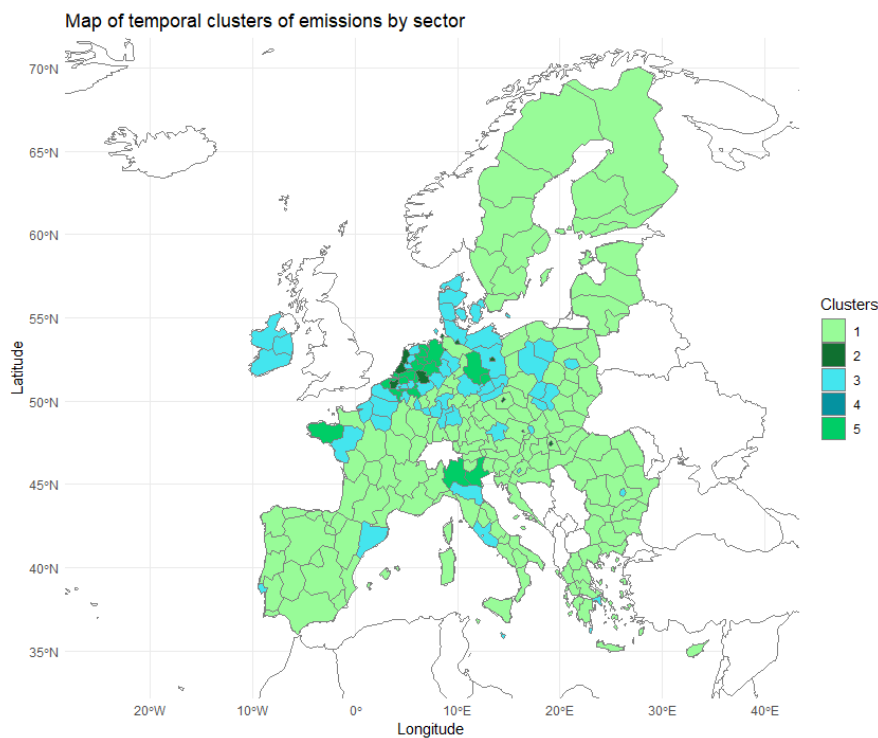


Fig. B3: Map of temporal clusters obtained combining the dissimilarity matrices of the time series of emissions of different sectors between 1990 and 2022.

a slight downward trend. Cluster 4 includes several metropolitan regions and displays the highest emission levels in the Buildings, Transport, and Waste sectors. Lastly, Cluster 5, primarily located in Northern Europe and Northern Italy, stands out as the largest emitter in the Agricultural sector.

Overall, our analysis confirms the significant relevance of the spatial component. Regions that are geographically close tend to exhibit similar emission patterns, both by gas type and sector. Incorporating the spatial component explicitly into the clustering algorithm produces groups that are more interpretable in terms of geographic proximity. This leads to results that are particularly valuable in environmental statistics, where spatiotemporal approaches and methodologies are essential for understanding and addressing complex phenomena.

References

Agrawal K, Garg S, Sharma S, et al (2016) Development and validation of OPTICS based spatio-temporal clustering technique. *Information Sciences* 369:388 – 401. <https://doi.org/10.1016/j.ins.2016.06.048>, URL <https://www.scopus.com/inward/record.uri?eid=2-s2.0-84977674847&>

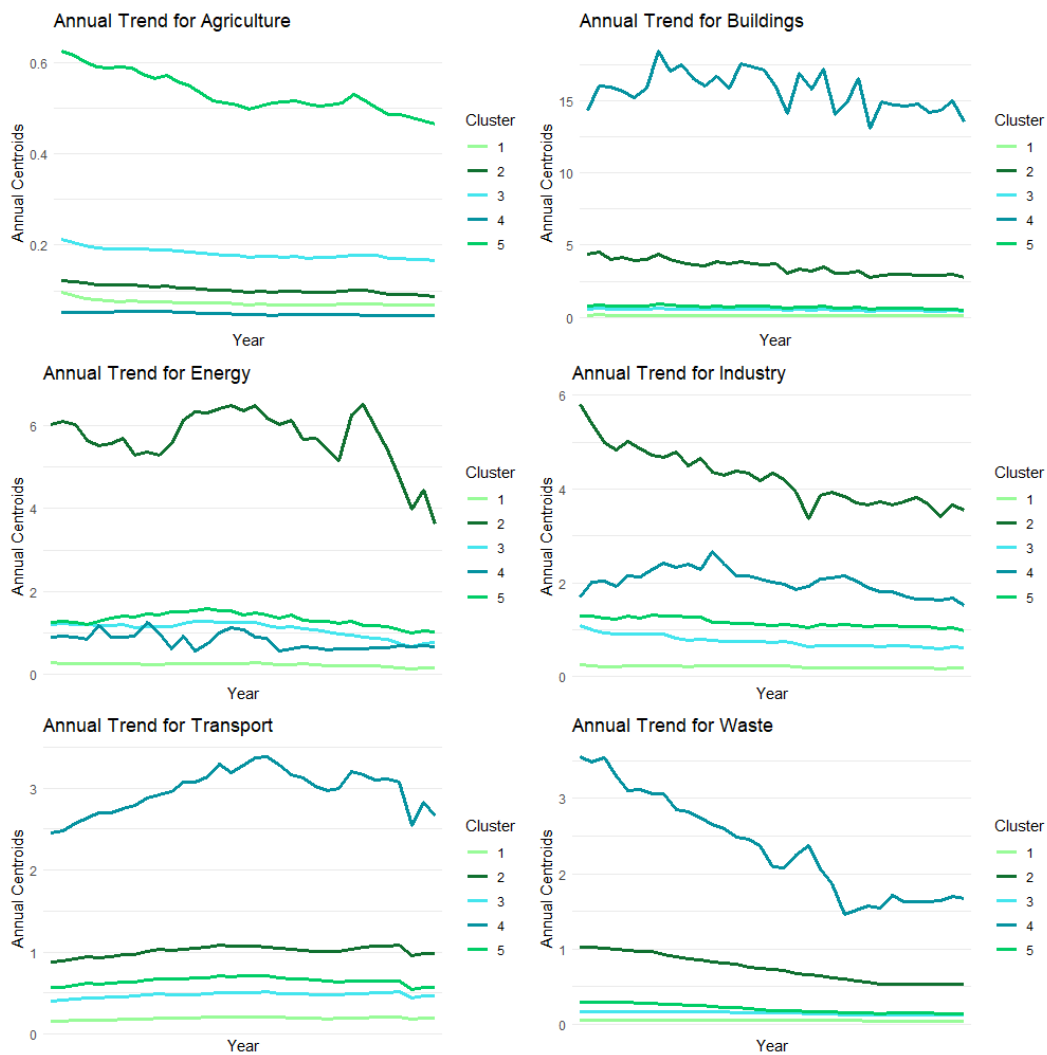


Fig. B4: Annual average of emission per km² of sectors for temporal clusters obtained combining the dissimilarity matrices of the time series of emissions of different sectors between 1990 and 2022.

[doi=10.1016%2fj.ins.2016.06.048&partnerID=40&md5=67b6c6447a1d4ac71cd0c1a5eea17e2d](https://doi.org/10.1016/j.ins.2016.06.048&partnerID=40&md5=67b6c6447a1d4ac71cd0c1a5eea17e2d)

Alatrística-Salas H, Azé J, Bringay S, et al (2015) A knowledge discovery process for spatiotemporal data: Application to river water quality monitoring. *Ecological Informatics* 26(P2):127 – 139. <https://doi.org/10.1016/j.ecoinf.2014.05.011>, URL <https://www.scopus.com/inward/record.uri?eid=2-s2.0-84939574642&doi=10.1016%2fj.ecoinf.2014.05.011&partnerID=40&md5=6138356b74699b12ee431e423030eccc>

- Ansari MY, Ahmad A, Khan SS, et al (2020) Spatiotemporal clustering: a review. *Artificial Intelligence Review* 53(4):2381 – 2423. <https://doi.org/10.1007/s10462-019-09736-1>, URL <https://www.scopus.com/inward/record.uri?eid=2-s2.0-85068956432&doi=10.1007%2fs10462-019-09736-1&partnerID=40&md5=e6852a2faff860d4938e522e3ebd9554>
- Berndt DJ, Clifford J (1994) Using dynamic time warping to find patterns in time series. *AAAIWS'94: Proceedings of the 3rd International Conference on Knowledge Discovery and Data Mining* pp 359–370
- Birant D, Kut A (2007) ST-DBSCAN: An algorithm for clustering spatial-temporal data. *Data and Knowledge Engineering* 60(1):208 – 221. <https://doi.org/10.1016/j.datak.2006.01.013>, URL <https://www.scopus.com/inward/record.uri?eid=2-s2.0-33846024749&doi=10.1016%2fj.datak.2006.01.013&partnerID=40&md5=8594c7a23a768f20115490fc091be556>
- Bucci A, Ippoliti L, Valentini P (2023) Analysing spatiotemporal patterns of COVID-19 confirmed deaths at the NUTS-2 regional level. *Regional Statistics* 13(2):214 – 239. <https://doi.org/10.15196/RS130202>, URL <https://www.scopus.com/inward/record.uri?eid=2-s2.0-85153956522&doi=10.15196%2fRS130202&partnerID=40&md5=e0caf54c37f055fbba4f7c0586f2ae93>
- Bucciarelli G (2024) ARDECO: Annual Regional Database of the European Commission (ARDECO). URL <https://CRAN.R-project.org/package=ARDECO>, r package version 2.1.0
- Calculli C, Fassò A, Finazzi F, et al (2015) Maximum likelihood estimation of the multivariate hidden dynamic geostatistical model with application to air quality in Apulia, Italy. *Environmetrics* 26(6):406–417. <https://doi.org/https://doi.org/10.1002/env.2345>, URL <https://onlinelibrary.wiley.com/doi/abs/10.1002/env.2345>
- Chavent M, Kuentz-Simonet V, Labenne A, et al (2018) ClustGeo: an R package for hierarchical clustering with spatial constraints. *Computational Statistics* 33:1 – 24. <https://doi.org/ff10.1007/s00180-018-0791-1>
- Chen XC, Faghmous JH, Khandelwal A, et al (2015) Clustering dynamic spatio-temporal patterns in the presence of noise and missing data. In: *IJCAI International Joint Conference on Artificial Intelligence*, p 2575 – 2581, URL <https://www.scopus.com/inward/record.uri?eid=2-s2.0>

0-84949815953&partnerID=40&md5=82c802d091285adb0ac115c82d0caa44

Crippa M, Guizzardi D, Solazzo E, et al (2024) Ghg emissions of all world countries - 2024. Report, Publications Office of the European Union, Luxembourg, <https://doi.org/10.2760/40028977, JRC138862>., URL <https://publications.jrc.ec.europa.eu/repository/handle/JRC138862>

Deb S, Karmakar S (2023) A novel spatio-temporal clustering algorithm with applications on COVID-19 data from the United States. Computational Statistics and Data Analysis 188. <https://doi.org/10.1016/j.csda.2023.107810>, URL <https://www.scopus.com/inward/record.uri?eid=2-s2.0-85162867311&doi=10.1016%2fj.csda.2023.107810&partnerID=40&md5=d7a1715870a1ad5cbf14818729e88f39>

Ester M, Kriegel HP, Sander J, et al (1996) A density-based algorithm for discovering clusters a density-based algorithm for discovering clusters in large spatial databases with noise. In: Proceedings - 2nd International Conference on Knowledge Discovery and Data Mining, KDD 1996, p 226 – 231, URL <https://www.scopus.com/inward/record.uri?eid=2-s2.0-85170282443&partnerID=40&md5=bbefa1633035b0779ae320a55ac5323a>

European Commission (2016) NUTS – Nomenclature of territorial units for statistics. <https://ec.europa.eu/eurostat/web/nuts>

Georgoulas G, Konstantaras A, Katsifarakis E, et al (2013) "seismic-mass" density-based algorithm for spatio-temporal clustering. Expert Systems with Applications 40(10):4183 – 4189. <https://doi.org/10.1016/j.eswa.2013.01.028>, URL <https://www.scopus.com/inward/record.uri?eid=2-s2.0-84875370729&doi=10.1016%2fj.eswa.2013.01.028&partnerID=40&md5=1264bd9bbf5f98ef8dd97a4bd069cf9e>

Gordon AD (1999) Classification. CRC Press

Jaya I, Ruchjana B, Andriyana Y, et al (2019) Clustering with spatial constraints: The case of diarrhea in Bandung city, Indonesia. In: Journal of Physics: Conference Series, <https://doi.org/10.1088/1742-6596/1397/1/012068>, URL <https://www.scopus.com/inward/record.uri?eid=2-s2.0-85078401440&doi=10.1088%2f1742-6596%2f1397%2f1%2f012068&partnerID=40&md5=ff7709958e63de22a0a3fa07a0711055>

- Jeung H, Yiu ML, Zhou X, et al (2008) Discovery of convoys in trajectory databases. In: Proceedings of the VLDB Endowment, p 1068 – 1080, <https://doi.org/10.14778/1453856.1453971>, URL <https://www.scopus.com/inward/record.uri?eid=2-s2.0-84859203289&doi=10.14778%2f1453856.1453971&partnerID=40&md5=a15cf61ea2c3c2a3c8887ef18d836814>
- Kalnis P, Mamoulis N, Bakiras S (2005) On discovering moving clusters in spatio-temporal data. In: Lecture Notes in Computer Science, p 364 – 381, https://doi.org/10.1007/11535331_21, URL https://www.scopus.com/inward/record.uri?eid=2-s2.0-26444541854&doi=10.1007%2f11535331_21&partnerID=40&md5=e2a4c78a8bca710454e8e6ba0a55985b
- Lee CH (2012) Mining spatio-temporal information on microblogging streams using a density-based online clustering method. *Expert Systems with Applications* 39(10):9623 – 9641. <https://doi.org/10.1016/j.eswa.2012.02.136>, URL <https://www.scopus.com/inward/record.uri?eid=2-s2.0-84862814748&doi=10.1016%2fj.eswa.2012.02.136&partnerID=40&md5=4582f880a00373dc3bb7643a4706dcee>
- Maranzano P, Fassó A (2022) The Impact of the Lockdown Restrictions on Air Quality During COVID-19 Pandemic in Lombardy, Italy. Springer, https://doi.org/10.1007/978-3-031-07155-3_15, URL https://www.scopus.com/inward/record.uri?eid=2-s2.0-85150925207&doi=10.1007%2f978-3-031-07155-3_15&partnerID=40&md5=596ef5a3bd958120c5e17c129fe5941e
- Maranzano P, Pelagatti M (2024) Spatiotemporal event studies for environmental data under cross-sectional dependence: An application to air quality assessment in Lombardy. *Journal of Agricultural, Biological, and Environmental Statistics* 29(1):147 – 168. <https://doi.org/10.1007/s13253-023-00564-z>, URL <https://www.scopus.com/inward/record.uri?eid=2-s2.0-85167788841&doi=10.1007%2fs13253-023-00564-z&partnerID=40&md5=382c633708b835c3f80aed8c521166eb>
- Maranzano P, Fassò A, Pelagatti M, et al (2020) Statistical modeling of the early-stage impact of a new traffic policy in milan, italy. *International Journal of Environmental Research and Public Health* 17(3). <https://doi.org/10.3390/ijerph17031088>, URL <https://www.scopus.com/inward/record.uri?eid=2-s2.0-85079309659&doi=10.3390%2fijerph17031088&partnerID=40&md5=df18f8e1769457e5d4cd6f9dfd25200b>

- Maranzano P, Otto P, Fassò A (2023) Adaptive LASSO estimation for functional hidden dynamic geostatistical models. *Stochastic Environmental Research and Risk Assessment* <https://doi.org/10.1007/s00477-023-02466-5>, URL <https://www.scopus.com/inward/record.uri?eid=2-s2.0-85169242030&doi=10.1007%2fs00477-023-02466-5&partnerID=40&md5=b0290bc5b274de3e33e24f49ad2c3e16>
- Mattera R, Franses PH (2023) Are African business cycles synchronized? Evidence from spatio-temporal modeling. *Economic Modelling* 128. <https://doi.org/10.1016/j.econmod.2023.106485>, URL <https://www.scopus.com/inward/record.uri?eid=2-s2.0-85169829326&doi=10.1016%2fj.econmod.2023.106485&partnerID=40&md5=2a9dbcc5024b0a4cad6b73062c9b3393>
- Morelli C, Boccaletti S, Maranzano P, et al (2025) Multidimensional spatiotemporal clustering - an application to environmental sustainability scores in europe. *Environmetrics* 36(2). <https://doi.org/10.1002/env.2893>, URL <https://www.scopus.com/inward/record.uri?eid=2-s2.0-85216969489&doi=10.1002%2fenv.2893&partnerID=40&md5=a350a71d40b156c892cf7e52579bff25>
- Naidu G, Zuva T, Sibanda EM (2023) A review of evaluation metrics in machine learning algorithms. In: *Artificial Intelligence Application in Networks and Systems*. Springer International Publishing, pp 15–25
- Najafabadi AM, Mahaki B, Hajizadeh Y (2020) Spatiotemporal modeling of airborne fine particulate matter distribution in isfahan. *International Journal of Environmental Health Engineering (IJEHE)* 2020(July):1–7. https://doi.org/10.4103/ijehe.ijehe_6_20
- Otto P, Fusta Moro A, Rodeschini J, et al (2024) Spatiotemporal modelling of PM 2.5 concentrations in Lombardy (Italy): a comparative study. *Environmental and Ecological Statistics* 31(2):245 – 272. <https://doi.org/10.1007/s10651-023-00589-0>, URL <https://www.scopus.com/inward/record.uri?eid=2-s2.0-85183928401&doi=10.1007%2fs10651-023-00589-0&partnerID=40&md5=7287355023438b6b6da56eeb4b8cf969>
- Rocha JAM, Times VC, Oliveira G, et al (2010) DB-SMoT: A direction-based spatio-temporal clustering method. In: *2010 IEEE International Conference on Intelligent Systems, IS 2010 - Proceedings*, p 114 – 119, <https://doi.org/10.1109/IS.2010.5548396>,

URL <https://www.scopus.com/inward/record.uri?eid=2-s2.0-77957843307&doi=10.1109%2fIS.2010.5548396&partnerID=40&md5=5b971c9788f4b2b97ee31908772d3134>

Sakoe H, Chiba S (1971) A dynamic programming approach to continuous speech recognition. Computer Science, Linguistics URL <https://api.semanticscholar.org/CorpusID:107516844>

Sakoe H, Chiba S (1978) Dynamic programming algorithm optimization for spoken word recognition. IEEE Transactions on Acoustics, Speech, and Signal Processing 26(1):43 – 49. <https://doi.org/10.1109/TASSP.1978.1163055>, URL <https://www.scopus.com/inward/record.uri?eid=2-s2.0-0017930815&doi=10.1109%2fTASSP.1978.1163055&partnerID=40&md5=214a08cd9889c7763a7eb3235d1718c6>

Taghavi-Shahri SM, Fassò A, Mahaki B, et al (2020) Concurrent spatiotemporal daily land use regression modeling and missing data imputation of fine particulate matter using distributed space-time expectation maximization. Atmospheric Environment 224. <https://doi.org/10.1016/j.atmosenv.2019.117202>, URL <https://www.scopus.com/inward/record.uri?eid=2-s2.0-85079163547&doi=10.1016%2fj.atmosenv.2019.117202&partnerID=40&md5=302b22fc3aaad92569abc95ec7d76ade>

Tietbohl A, Bogorny V, Kuijpers B, et al (2008) A clustering-based approach for discovering interesting places in trajectories. In: Proceedings of the ACM Symposium on Applied Computing, p 863 – 868, <https://doi.org/10.1145/1363686.1363886>, URL <https://www.scopus.com/inward/record.uri?eid=2-s2.0-56749150055&doi=10.1145%2f1363686.1363886&partnerID=40&md5=d2a6a24e973393a25daf0fd75145141f>

Vieira MR, Bakalov P, Tsotras VJ (2009) On-line discovery of flock patterns in spatio-temporal data. In: GIS: Proceedings of the ACM International Symposium on Advances in Geographic Information Systems, p 286 – 295, <https://doi.org/10.1145/1653771.1653812>, URL <https://www.scopus.com/inward/record.uri?eid=2-s2.0-74049140321&doi=10.1145%2f1653771.1653812&partnerID=40&md5=af9ade16306a187ac63f360d2017939a>

Wang M, Wang A, Li A (2006) Mining spatial-temporal clusters from geo-databases. Lecture Notes in Computer Science (including subseries Lecture Notes in Artificial Intelligence and

Lecture Notes in Bioinformatics) 4093 LNAI:263 – 270. https://doi.org/10.1007/11811305_29, URL https://www.scopus.com/inward/record.uri?eid=2-s2.0-33749420928&doi=10.1007%2f11811305_29&partnerID=40&md5=3012719c1262feebc3f07af280141a26

Ward JH (1963) Hierarchical grouping to optimize an objective function. Journal of the American Statistical Association 58(301):236 – 244. <https://doi.org/10.1080/01621459.1963.10500845>, URL <https://www.scopus.com/inward/record.uri?eid=2-s2.0-84944178665&doi=10.1080%2f01621459.1963.10500845&partnerID=40&md5=b7ae8f33de94c451f20275ab517ada5d>

Zammarchi G, Maranzano P (2024) Mapping climate change awareness through spatial hierarchical clustering. URL <https://arxiv.org/pdf/2409.13760>, 2409.13760